

AD-A193 205

THIN FILM-RESIDUAL STRESS ASSESSMENT(U) AEROSPACE CORP  
EL SEGUNDO CA MATERIALS SCIENCES LAB D J CHANG ET AL  
12 FEB 88 TR-0086A(2935-12)-3 SD-TR-88-28  
F04701-85-C-0086

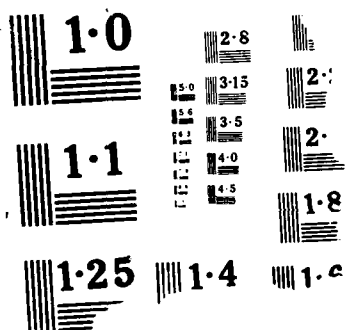
1/1

UNCLASSIFIED

F/G 11/3

NL

00  
00



(4)

AD-A193 205

## Thin Film-Residual Stress Assessment

D. J. CHANG, R. MUKI, P. M. ADAMS, K. W. PASCHEN, and C. TSENG  
Materials Sciences Laboratory  
Laboratory Operations  
The Aerospace Corporation  
El Segundo, CA 90245

12 February 1988

Prepared for  
SPACE DIVISION  
AIR FORCE SYSTEMS COMMAND  
Los Angeles Air Force Base  
P.O. Box 92960, Worldway Postal Center  
Los Angeles, CA 90009-2960

APPROVED FOR PUBLIC RELEASE.  
DISTRIBUTION UNLIMITED

DTIC  
SELECTED  
APR 13 1988  
H

This report was submitted by The Aerospace Corporation, El Segundo, CA 90245, under Contract No. F04701-85-C-0086 with the Space Division, P.O. Box 92960, Worldway Postal Center, Los Angeles, CA 90009-2960. It was reviewed and approved for The Aerospace Corporation by R. W. Fillers, Director, Materials Sciences Laboratory.

Lt Constance M. Chintall/CNIV was the project officer for the Mission-Oriented Investigation and Experimentation (MOIE) Program.

This report has been reviewed by the Public Affairs Office (PAS) and is releasable to the National Technical Information Service (NTIS). At NTIS, it will be available to the general public, including foreign nationals.

This technical report has been reviewed and is approved for publication. Publication of this report does not constitute Air Force approval of the report's findings or conclusions. It is published only for the exchange and stimulation of ideas.

*Constance M. Chintall*

CONSTANCE M. CHINTALL, Lt, USAF  
MOIE Project Officer  
SD/CNIV

*Raymond M. Leong*

RAYMOND M. LEONG, Major, USAF  
Deputy Director, AFSTC West Coast Office  
AFSTC/WCO OL-AB

UNCLASSIFIED

SECURITY CLASSIFICATION OF THIS PAGE

## REPORT DOCUMENTATION PAGE

1a. REPORT SECURITY CLASSIFICATION Unclassified			1b. RESTRICTIVE MARKINGS		
2a. SECURITY CLASSIFICATION AUTHORITY			3. DISTRIBUTION / AVAILABILITY OF REPORT Approved for public release; distribution unlimited		
2b. DECLASSIFICATION / DOWNGRADING SCHEDULE					
4. PERFORMING ORGANIZATION REPORT NUMBER(S) TR-0086A(2935-12)-3			5. MONITORING ORGANIZATION REPORT NUMBER(S) SD-TR-88-28		
6a. NAME OF PERFORMING ORGANIZATION The Aerospace Corporation Laboratory Operations		6b. OFFICE SYMBOL (if applicable)		7a. NAME OF MONITORING ORGANIZATION Space Division	
6c. ADDRESS (City, State, and ZIP Code) El Segundo, CA 90245			7b. ADDRESS (City, State, and ZIP Code) Los Angeles Air Force Base Los Angeles, CA 90009-2960		
8a. NAME OF FUNDING / SPONSORING ORGANIZATION		8b. OFFICE SYMBOL (if applicable)		9. PROCUREMENT INSTRUMENT IDENTIFICATION NUMBER F04701-85-C-0086-P00016	
8c. ADDRESS (City, State, and ZIP Code)			10. SOURCE OF FUNDING NUMBERS		
			PROGRAM ELEMENT NO	PROJECT NO	TASK NO
			WORK UNIT ACCESSION NO		
11. TITLE (Include Security Classification) Thin Film-Residual Stress Assessment					
12. PERSONAL AUTHOR(S) Chang, D. J., Muki, R., Adams, P. M., Paschen, K. W., and Tseng, C.					
13a. TYPE OF REPORT		13b. TIME COVERED FROM TO		14. DATE OF REPORT (Year, Month, Day) 1988 February 12	
				15. PAGE COUNT 77	
16. SUPPLEMENTARY NOTATION					
17. COSATI CODES			18. SUBJECT TERMS (Continue on reverse if necessary and identify by block number)		
FIELD	GROUP	SUB-GROUP	Laser interferometry ; Shear modulus		
			Stress behavior ; Thermal stress		
			Young's modulus ; Intrinsic stress		
19. ABSTRACT (Continue on reverse if necessary and identify by block number) That residual stresses exist in thin-film coated structures has been known for decades. Their existence plays an important role in the ability of coated structures to withstand external loads which might arise from mechanical, thermal, electrical and optical environments. Magnitudes of the residual stresses are influenced by many factors. These include mechanical properties of the films and substrates, mismatch of the thermal expansion between films and substrates, processing parameters such as deposition rate, film thickness, substrate temperature and chamber pressure during deposition, and coating/substrate adhesion characteristics.  A successful prediction of residual stresses relies on; (1) valid mathematical modeling, (2) accurate measurement of deformation of thin film coated structures, (3) detailed understanding of the mechanical and thermophysical properties of the films and substrate materials. This report documents the result, findings, progress and status of the residual stress assessment activities in the following categories: (1) Analytical, derivation of					
20. DISTRIBUTION / AVAILABILITY OF ABSTRACT <input checked="" type="checkbox"/> UNCLASSIFIED UNLIMITED <input type="checkbox"/> SAME AS RPT <input type="checkbox"/> DTIC USERS			21. ABSTRACT SECURITY CLASSIFICATION Unclassified		
22a. NAME OF RESPONSIBLE INDIVIDUAL			22b. TELEPHONE (Include Area Code)		22c. OFFICE SYMBOL

UNCLASSIFIED

SECURITY CLASSIFICATION OF THIS PAGE

19. Continued

stress behavior in the film coated substrates, (2) development of viable measuring techniques to determine the deformation of thin film coated structures, (3) establishment of a testing methodology to quantify the coating material properties in thin film configurations, and (4) identification of failure modes and failure mechanisms to provide information toward the establishment of failure criteria of thin film coated structures.

*Page 19*

UNCLASSIFIED  
SECURITY CLASSIFICATION OF THIS PAGE

# CONTENTS

I.	RESIDUAL STRESS ASSESSMENT.....	5
II.	ANALYTICAL DERIVATION OF STRESS BEHAVIOR.....	9
	A. Residual Stress in Thin Films.....	9
	B. Intrinsic and Thermal Stresses in Substrate During Coating Deposition.....	14
III.	DEVELOPMENT OF DEFORMATION MEASURING TECHNIQUES.....	23
	A. Laser Interferometry.....	23
	B. X-ray Diffraction.....	37
	C. Differential Capacitance.....	51
IV.	MATERIAL PROPERTY DETERMINATION.....	57
	A. Determination of Young's Modulus.....	57
	B. Determination of Shear Modulus.....	64
	REFERENCES .....	69

Accession For	
NTIS GRA&I	<input checked="" type="checkbox"/>
DTIC TAB	<input type="checkbox"/>
Unannounced	<input type="checkbox"/>
Justification	
By	
Distribution/	
Availability Codes	
Dist	Avail and/or Special
A-1	

## FIGURES

1.	One-Dimensional Heat Conduction.....	16
2.	Nondimensional Temperature History of Substrate.....	18
3.	Nondimensional Temperature During Deposition Across the Substrate for Various Times.....	19
4.	Deflections Versus Time in Cantilever Substrate.....	21
5.	Michelson Interferometer.....	24
6.	Tilted Sample.....	26
7.	Spherical Sample.....	27
8.	Tilt Correction.....	28
9.	Substrate Mount.....	30
10.	Normalized Pressure Contribution.....	33
11.	Interferograms.....	36
12.	Displacement Versus Temperature.....	38
13.	Diffractometer Setting.....	40
14.	X-ray Rocking Curve of Unstressed Silicon Wafer.....	42
15.	X-ray Rocking Curve of Sample B, $L = 1.77$ cm.....	43
16.	Schematic of Wafer Configuration.....	45
17.	Slope and Slope Difference of Wafer Versus X-ray Location for $L = 1$ cm.....	45
18.	Slope and Slope Difference of Wafer Versus X-ray Location for $L = 1.7$ cm.....	46
19.	Slope and Slope Difference of Wafer Versus X-ray Location for $L = 2$ cm.....	46
20.	X-ray Rocking Curve of Sample B, $L = 3.01$ cm.....	49
21.	X-ray Rocking Curve of Sample C, $L = 2.30$ cm.....	49



## FIGURES (Continued)

22.	Frequency Ratio Versus Modulus Ratio, $d_f/d_s = 3.58 \times 10^{-04}$ .....	61
23.	Frequency Ratio Versus Modulus Ratio $d_f/d_s = 7.16 \times 10^{-04}$ .....	62
24.	Frequency Ratio Versus Modulus Ratio $d_f/d_s = 1.07 \times 10^{-03}$ .....	63
25.	Geometry and Coordinates.....	65

## TABLES

1.	Intrinsic Stresses in Dielectric Films Approximately 5000 Å Thick.....	6
2.	Intrinsic Stresses in Metal Films Approximately 1000 Å Thick.....	7
3.	Radius of Curvature and Deflection Data Determined from XRD and Laser Interferometry.....	50
4.	Comparison Between Laser Interferometry and Capacitance Methods.....	55
5.	Material Properties.....	60

## I. RESIDUAL STRESS ASSESSMENT

The existence of the residual stresses in thin-film coated structures has attracted the interest of many investigators. The study of the residual stress behavior on evaporated films was first performed by Stoney<sup>(1)</sup> as early as 1909. He derived a simplified, although inaccurate, expression for the stress in a thin film deposited on a substrate strip based on the elastic theory of simple beams. Since then, more work has been done by Hoffman,<sup>(2)</sup> Finegan,<sup>(3)</sup> Brenner and Sanderoff<sup>(4)</sup> to refine the stress prediction techniques.

However, the residual stress prediction technology depends on accurate measurements of the geometric deformation of the thin-film coated structures. The film stress can be tensile or compressive depending on the mechanical properties of the films and substrates such as the Young's moduli, magnitude of the mismatch of the thermal expansion between film and substrate, the processing parameters such as deposition rate, film thickness, substrate temperature and chamber pressure during deposition, and the coating/substrate adhesion characteristics. Deformation of the structures such as change of local radius of curvature, strains, deflections, etc. will be induced due to the residual stresses existing in the structure.

Tables 1 and 2, taken from Ref. 2, summarize the currently available stress data for dielectric and metallic films on a variety of substrates. These data provide some insight of both the residual stress behavior and their magnitudes which may be expected in a thin-film coating. Furthermore, the mechanical properties of the thin-film coating dictate the type (tension or compression) and the magnitude of the residual stresses in a thin film. Coatings often exhibit properties which may differ significantly from their bulk properties. Hence, one would need to measure the mechanical properties of coating materials in the thin-film configuration. The properties needed include Young's modulus, shear modulus, free thermal expansion, and thermal conductivity as functions of temperature.

Table 1. Intrinsic Stresses in Dielectric Films Approximately 5000 Å Thick  
(from Ref. 2)

Material	Substrate Temp. (°C) <sup>a</sup>	Substrate Material	Stress (10 <sup>9</sup> dyne/cm <sup>2</sup> ) <sup>b</sup>	Sign <sup>c</sup>	Method <sup>d</sup>
ZnS	110	Glass	1.0	C	C
	A	Glass	(0.002)	C	C
	A	Mica		C	C
SiO	110	Glass	1.2	C	C
	A	Nickel	4	T	C
MgF <sub>2</sub>	110	Glass	2.0	T	B
	75	Mica	2.2	T	B
	A	Glass	(0.11)	T	C
	A	Mica	(0.11)	T	C
	A	Glass	1	T	
LiF	110	Glass	0.4	T	C
	A	Cellulose	2.0	T	ED
	A	Glass	0.28	T	
	A	Mica	(0.023)	T	C
	A	Glass	(0.023)	T	C
CaF <sub>2</sub>	110	Glass	0.2	T	C
	A	Mica	(<0.0003)	T	C
	A	Glass	(None)		C
Cryolite	A	Glass	(0.061)	T	C
	A	Glass	(0.06)	T	C
	A	Glass	0.5	T	
PbCl <sub>2</sub>	50	Glass	0.18	T	C
	A	Glass	(0.014)	T	C
PbF <sub>2</sub>	110	Glass	0.8	T	C
AgCl	A	Glass	(None)		C
AgF	A	Glass	(None)		C
AgI	A	Glass	(None)		C
BaF <sub>2</sub>	A	Glass	(0.006)	T	C
BaO	50	Glass	0.15	C	C
Sb <sub>2</sub> O <sub>3</sub>	A	Glass	(0.007)	T	C
Sb <sub>2</sub> S <sub>3</sub>	A	Glass	(0.007)	T	C
Ce <sub>2</sub> O <sub>3</sub>	50	Glass	1.6	C	C
CeF <sub>3</sub>	40	Glass	2.8	T	C
CdS	110	Glass	0.8	C	C
SnO <sub>2</sub>	A	Glass	(0.008)	T	C
C	A	Glass	4.0	C	C
NaF	A	Glass	0.1	T	
B <sub>2</sub> O <sub>3</sub>	90	Glass	0.1	T	C
Chiolite	A	Glass	(0.029)	T	C
AlPh <sup>e</sup>	40	Glass	0.6	C	C
MgPh <sup>e</sup>	40	Glass	0.6	C	C
MoO <sub>3</sub>	A	Glass	(0.013)	T	C
CuI	A	Glass	(None)		C
Alf <sub>3</sub>	A	Glass	(None)		C
SrSO <sub>4</sub>	A	Glass	(None)		C

<sup>a</sup>A, thermally floating at ambient temperature.

<sup>b</sup>Values in parentheses are relative.

<sup>c</sup>C and T, compression or tension.

<sup>d</sup>B, end-supported beam; C, cantilever beam; and ED, electron-diffraction technique.

<sup>e</sup>Al and Mg thalocyanine.

Table 2. Intrinsic Stresses in Metal Films Approximately 1000 Å Thick  
(from Ref. 2)

Material	Substrate Temp. (°C) <sup>a</sup>	Substrate Material	Stress (10 <sup>9</sup> dyne/cm <sup>2</sup> )	Sign <sup>b</sup>	Method <sup>c</sup>
Ag	90	Glass	0.75	T	C
	A	Copper	1.0	T	T
	A	Mica	0.2	T	C
	A	Copper	0.75	T	C
Al	A	Cellulose	1.2	T	ED
	A	Copper	0.1	T	C
Au	A	Cellulose	4.6	T	ED
	A	Quartz	2.9	T	P
	A	Copper	0.85	T	C
Cu	A	Copper	0.9	T	C
	25	Mica	0.2	T	B
	A	Cellulose	4.4	C	ED
	A	Copper	1.5	T	C
	75	Mica	0.1	T	C
	-150	Mica	3.6	T	C
Ni	A	Glass	5-8	T	P
	A	Copper	3.5	T	C
	A	Glass	7.7	T	C
	75	Mica	6.4	T	B
	175	Mica	2.6	T	B
	A	Mica	5-8	T	FR
Fc	75	Mica	10.5 <sup>d</sup>	T	B
	175	Mica	5.9 <sup>d</sup>	T	B
	75+A	Glass	9.6 <sup>d</sup>	T	P
	A	Glass,Silica	8.5 <sup>e</sup>	T	P
	A	Copper	3.1	T	C
Permalloy	75	Glass	9	T	P
	75	Glass,Mica	9	T	C
Sb	A	Copper	0.8	T	C
	A	Copper	0.25	T	C
Co	200	Glass	3.4	T	B
Pd	A	Copper	1.4	T	C
Mg	A	Copper	0		C
Bi	A	Copper	0		C
Zn	A	Copper	0		C
Pb	A	Nickel	0		C
Sn	A	Glass	0		C
In	A	Silica	0		C

<sup>a</sup>A means thermally floating at ambient temperature.

<sup>b</sup>T refers to tension, C to compression.

<sup>c</sup>B, beam supported on both ends; C, cantilever beam; ED, electron diffraction; and FR, ferromagnetic resonance.

<sup>d</sup>Poisson-corrected.

<sup>e</sup>Poisson-corrected, 36.5° angle of incidence.

Failure or degradation of thin films as a result of either the deposition process, or under external mechanical and thermal loadings, requires a detailed and systematic investigation. Failures may include local cracking, wrinkling, spallation, melting, and sublimation. These failures can be generated by thermal stress or mechanical stress, or a combination of the two. Detailed investigations are hence needed to identify the failure modes and failure mechanisms in order to provide guidelines to enhance the predictability of the response of thin coatings under given external mechanical, laser, or nuclear environments.

Therefore, the activities of the residual stress assessment task of the program include:

1. Analytical derivation of stress behavior in thin film coated substrates
2. Development of viable measuring techniques to determine the deformation of thin film coated structures
3. Establishment of a testing methodology to quantify coating material properties in thin film configurations
4. Identification of failure modes and failure mechanisms to provide information toward the establishment of failure criteria of thin film coated structures

The results and the progress of each of the above activities are discussed in the following sections.

## II. ANALYTICAL DERIVATION OF STRESS BEHAVIOR

### A. RESIDUAL STRESS IN THIN FILMS

Stoney's original problem was re-evaluated to clarify the underlying assumptions and to identify problem areas that were needed for thorough understanding of residual stress distribution in films of thickness  $t$ . The model includes a planar substrate of thickness  $d$  and a typical linear dimension  $l$ . During the course of the film deposition, the substrate undergoes deformation. The deformation is composed of two sources: thermally induced and non-thermally induced. The former is caused by the temperature rise and the temperature gradient associated with the film deposition, while the latter is caused by the atomic interaction between the film and substrate materials. At post vacuum, the temperature of the film-substrate assembly returns to ambient conditions and the thermally induced deformation disappears. The deformation of the system is therefore due to the "non-thermally induced" stress as a result of film deposition. This stress is defined as "intrinsic stress". Therefore, the intrinsic stress is regarded as the level of stress which exists in the system as a result of the film deposition without any boundary constraint to the system. Therefore, any thermal gradient-induced stresses and stresses associated with boundary condition changes are not included in the intrinsic stress. The general case as well as those for both cantilever strips and circular disks are considered.

The following assumptions are adopted:

1. The substrate material is homogeneous, isotropic and linearly elastic with Young's modulus  $E$  and Poisson's ratio  $\nu$ .
2.  $t \ll d \ll l$
3. The edge of the assembly is traction-free.
4. The bond between the film and the substrate is perfect.
5. The film experiences an average two-dimensional hydrostatic state of stress which is uniform throughout the film thickness. This average intrinsic stress is denoted by  $S$ .

Take cartesian coordinates  $x, y, z$  with the plane  $z = 0$  coinciding with the central plane of the substrate. Therefore, the coordinate  $z$  runs across the thickness direction of the substrate. These assumptions apply to the case where the substrate is subjected to a state of spherical bending. Thus, one has the in-plane linear stress components  $\sigma_{xx}(z), \sigma_{yy}(z)$  as

$$\sigma_{xx}(z) = \sigma_{yy}(z) \equiv \sigma(z) \quad (1)$$

$$\sigma_{ij} = 0 \text{ otherwise } (i, j: x, y, z)$$

and the in-plane linear strains  $\epsilon_{xx}(z)$  and  $\epsilon_{yy}(z)$  obey

$$\epsilon_{xx}(z) = \epsilon_{yy}(z) = \epsilon(z) = \epsilon(z) = -\frac{c+z}{r} = \frac{1-\nu}{E} \sigma(z) \quad (2)$$

where  $r$  is the radius of curvature of the neutral plane and  $c$  is the distance of the neutral plane from the plane  $z = 0$ . From Eq. (2) the stress in the substrate can be expressed as

$$\sigma(z) = -\frac{E}{1-\nu} \frac{c+z}{r}$$

The requirement of force and moment equilibrium over the cross section provides

$$\int_{d/2}^{d/2+t} S dz + \int_{-d/2}^{d/2} \sigma(z) dz = St - \frac{CdE}{(1-\nu)r} = 0$$

$$\int_{d/2}^{d/2+t} S z dz + \int_{-d/2}^{d/2} \sigma(z) z dz = \frac{S}{2} t(t+d) - \frac{cd^3E}{12(1-\nu)r} = 0$$

The film stress  $S$  and the distance  $c$  between the neutral and middle plane are therefore solved as

$$S = \frac{d^3 E}{6(1 - \nu)t(d + t)r} \doteq \frac{d^2 E}{6(1 - \nu)tr} \quad (3)$$

$$c = \frac{d^2}{6(d + t)} \doteq \frac{d}{6}$$

Denote the displacement in z-direction of a point on the neutral plane by  $\omega$  and let

$$\omega = 0 \quad \frac{\partial \omega}{\partial x} = \frac{\partial \omega}{\partial y} = 0 \quad \text{at } x = y = 0.$$

Since the deformation  $\omega$  is axisymmetric with respect to the z axis, let's consider  $\omega$  along the x-axis which, in view of the first of Eq. (3), permits the expression:

$$\omega(x, 0) = r - (r^2 - x^2)^{1/2} \doteq \frac{x^2}{2r} = \frac{3(1 - \nu)t S}{Ed^2} x^2 \quad (4)$$

By use of Eq. (4), the film stress  $S$  can be evaluated from:

1. The end deflection  $\delta_c$  of a cantilever beam of length  $l$
2. The relative deflection  $\delta_s$  between the center and the support of a simply supported beam of length  $l$
3. The relative deflection  $\delta_{sd}$  between the center and the support of a simply supported disk of diameter  $l$

In particular, for a cantilever strip the average film stress is

$$S = \frac{Ed^2 \delta_c}{3(1 - \nu)t l^2} \quad (5)$$

Further,  $\delta_c$ ,  $\delta_s$  and  $\delta_{sd}$  for the same film stress are related by

$$\delta_c = 4\delta_s = 4\delta_{sd} \quad (6)$$



Next consider a beam clamped at both ends and a circular disk clamped along the periphery. Since the substrate is subjected to isotropic bending, the application of additional moment at the boundaries to satisfy the zero-slope condition makes the deflection of the entire beam or disk vanish.

The intrinsic stress distribution across the film thickness can be determined by use of the above equations. Suppose that the intrinsic stress  $\sigma_f$  in the film depends on the distance  $t$  from the substrate. Then the average stress  $S$  is related to  $\sigma_f$  by

$$tS(t) = \int_0^t \sigma_f(s) ds \quad (7)$$

If  $\sigma_f$  at a given point does not vary with the film thickness, we can differentiate Eq. (7) to obtain

$$\sigma_f(t) = S(t) + tS'(t) \quad (8)$$

The expression (Eq. 8) enables us to find the distribution of  $\sigma_f$  approximately if the average stress  $S(t)$  is measured for several film thicknesses.

Stresses in the film-substrate assembly consistent with Stoney's formula are written from Eqs. (1), (2), and (3) as follows.

Film (superscript  $f$ )

$$\begin{aligned} \sigma_{xx}^f(z) = \sigma_{yy}^f(z) = \sigma^f(z) = S \\ \sigma_{ij}^f = 0 \quad \text{otherwise} \quad \left(\frac{d}{2} < z < \frac{d}{2} + t\right) \end{aligned}$$

Substrate (superscript  $S$ )

$$\begin{aligned} \sigma_{xx}^S(z) = \sigma_{yy}^S(z) = \sigma^S(z) = -\frac{6St}{d^2} \left(z + \frac{d}{6}\right) \\ \sigma_{ij}^S = 0 \quad \text{otherwise} \quad \left(-\frac{d}{2} < z < \frac{d}{2}\right) \end{aligned} \quad (9)$$

Based on the assumptions and Eqs. (1) through (3), one can also obtain the stress field at the film-substrate interface which is valid at the interior of the assembly.

$$\sigma_{xz}^f = \sigma_{yz}^f = \sigma_{zz}^f = 0 \quad (10)$$

$$\sigma_{xz} = \sigma_{yz} = \sigma_{zz} = 0 \quad \text{at } z = d/2$$

However, at the free end of the substrate, there is a boundary layer on the order of the film thickness in extent, within which non-zero normal and shear stresses exist over the film-substrate interface. The exact solution to this problem is obtainable by use of classical theory of elasticity though the analysis is expected to be involved and time-consuming.

Reference 5 provides the behavior of the normal and shear stress fields within the region of the boundary layer for a single lap joint under the application of uniaxial tension at far field. Although the exact stress distributions at the end of the film-substrate interface within the boundary layer differ from that in a single lap joint, the general singularity is similar. In both cases, the normal bond stress for the lap joint is highly localized and changes sign with its net force over the entire bond line vanishing as it should. A similar normal stress distribution is expected for the current problem. Shear stress on the interface is also expected to be highly localized.

The above derivation is valid when the thickness of the substrate is small enough such that it will undergo a change of radius of curvature. When the substrate is thick enough such that no measurable substrate deformation can be made, there is a concern as to the magnitude of the intrinsic stress in the coating in comparison to that in a thin substrate.

At  $z = d/2$ , the plane where the film is deposited, the strain  $\epsilon(z)$  is expressed as

$$\epsilon\left(\frac{d}{2}\right) = -\frac{2d}{3r} \quad (11)$$

This strain needs to be removed when the substrate is very thick. Consequently, it is equivalent to apply a stress of  $\Delta S_f$  of a magnitude equal to

$$\Delta S_f = \frac{2}{3} \frac{E_f}{1 - \nu} \frac{d}{r} \quad (12)$$

When this compares with the average film stress  $S$ , it is found that

$$\Delta S_f = 4 \frac{t}{d} \frac{E_f}{1 - \nu_f} \frac{1 - \nu}{E} S \quad (13)$$

which implies that

$$\Delta S_f = o\left(\frac{t}{d} S\right)$$

since  $\frac{t}{d} \ll 1$ , unless  $\frac{E_f}{1 - \nu_f}$  is substantially larger than  $\frac{E}{1 - \nu}$ . The small "o" symbol is used to indicate that the ratio of  $\Delta S_f$  to  $\frac{t}{d} S$  is very small. Therefore, it is concluded that the dependence of the intrinsic stress upon the substrate thickness is negligible unless the film modulus is much greater than the substrate modulus.

#### B. INTRINSIC AND THERMAL STRESSES IN SUBSTRATE DURING COATING DEPOSITION

Both intrinsic and thermal stresses develop during a film deposition. The intrinsic stress is due to the atomic interaction between the substrate and coating materials. The thermal stress develops due to the temperature gradient associated with the deposition process. The temperature difference across the substrate is generally very small ( $< 0.1^\circ\text{C}$ ) because of the thinness of the substrate. This difference is generally disregarded by assuming a constant temperature throughout the substrate/coating assembly in most of the analytical work. This assumption may lead to an incorrect deformation prediction for the intrinsic stress calculation. This is because the in-situ or post deposition measurements include both the intrinsic stress and the thermal stress deformations. If the latter part of the deformation is not

negligible relative to the former one, an inaccurate intrinsic stress would be predicted. A thermal deflection analysis for a thin film deposited on a plate under a uniform heat flux was performed since a direct prediction of the intrinsic stress induced deformation is difficult to achieve. Blackburn and Campbell<sup>(6)</sup> published an in-situ displacement measurement of LiF deposited on a glass cantilever strip. There appeared to be a sudden jump at the beginning and a sudden drop at the end of deposition. This deviation from a smooth curve has not been resolved. It was hoped that the discrepancy could be explained analytically so that this data could be used to correlate with our analytical predictions.

Temperature distributions in the substrate during and after coating deposition are well represented by solutions to the one-dimensional heat conduction problem of a slab bounded by two planes,  $z = 0$  and  $z = d$  (Fig. 1). At the initial instant, the temperature  $T(z,t)$ , where  $t$  is the time variable, is equal to the ambient temperature  $T_0$ . During the film deposition, we assume that a constant rate of heat flux  $q_0$  per unit area is supplied at the front surface and heat radiates at the rear surface into the surrounding medium of temperature  $T_0$  according to Newton's law, with coefficient of surface heat transfer  $H$ . Once deposition is ended, the heat is assumed to radiate from the front and rear planes with a linear initial temperature distribution.

To simplify the formulation of the analysis, we introduce the following dimensionless quantities:

$$\begin{aligned}\xi &= z/d \\ \tau &= \kappa t/d^2 \\ \epsilon &= dH/K \\ v(\xi, \tau) &= [T(z,t) - T_0]/[T_1 - T_0] \\ \theta_0 &= dq_0/[K(T_1 - T_0)] \quad (14)\end{aligned}$$

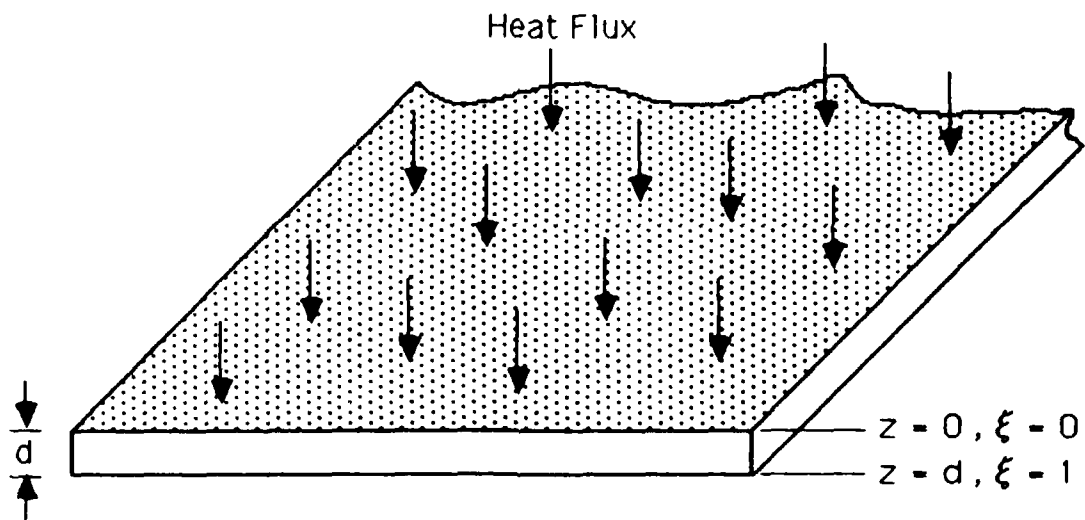


Fig. 1. One-Dimensional Heat Conduction

where  $K$  is the substrate conductivity,  $\kappa$  is the substrate diffusivity, and  $T_1$  denotes the equilibrium temperature at the front surface when the deposition is continued indefinitely.

In this dimensionless formulation, the heat conduction equation

$$\frac{\partial^2 v}{\partial \xi^2} = \frac{\partial v}{\partial \tau} \quad (0 < \xi < 1, \quad 0 < \tau < \infty) \quad (15)$$

is accompanied, for the deposition problem, by the boundary conditions

$$\begin{aligned} v_d(\xi, 0) &= 0 & (0 < \xi < 1), \\ \frac{\partial v_d}{\partial \xi} + \beta_0 &= 0 & \text{at } \xi = 0, \\ \frac{\partial v_d}{\partial \xi} + \epsilon v_d &= 0 & \text{at } \xi = 1; \end{aligned} \quad (16)$$

and similarly, for the post-deposition problem, by

$$\begin{aligned} v_p(\xi, 0) &= a + b\xi & (0 < \xi < 1), \\ \frac{\partial v_p}{\partial \xi} - \epsilon v_p &= 0 & \text{at } \xi = 0, \\ \frac{\partial v_p}{\partial \xi} + \epsilon v_p &= 0 & \text{at } \xi = 1. \end{aligned} \quad (17)$$

where  $v_d$  and  $v_p$  correspond to the normalized temperature fields for the deposition and post-deposition problems. For the detailed derivation of solutions to Eqs. (15) through (17), refer to Appendix A.

The non-dimensional temperature fields of the heated surface during and after deposition are depicted in Fig. 2 based on the thermal conductivity, specific heat of the substrate, and the geometric dimensions of the cantilever strip. The temperature distributions versus substrate thickness are depicted in Fig. 3 for several different time values. They correspond to a temperature difference between the heated and the unheated surfaces of  $0.0061^\circ\text{C}$  at  $t = 0.1$  sec and  $0.0096^\circ\text{C}$  at  $t = 100$  sec.

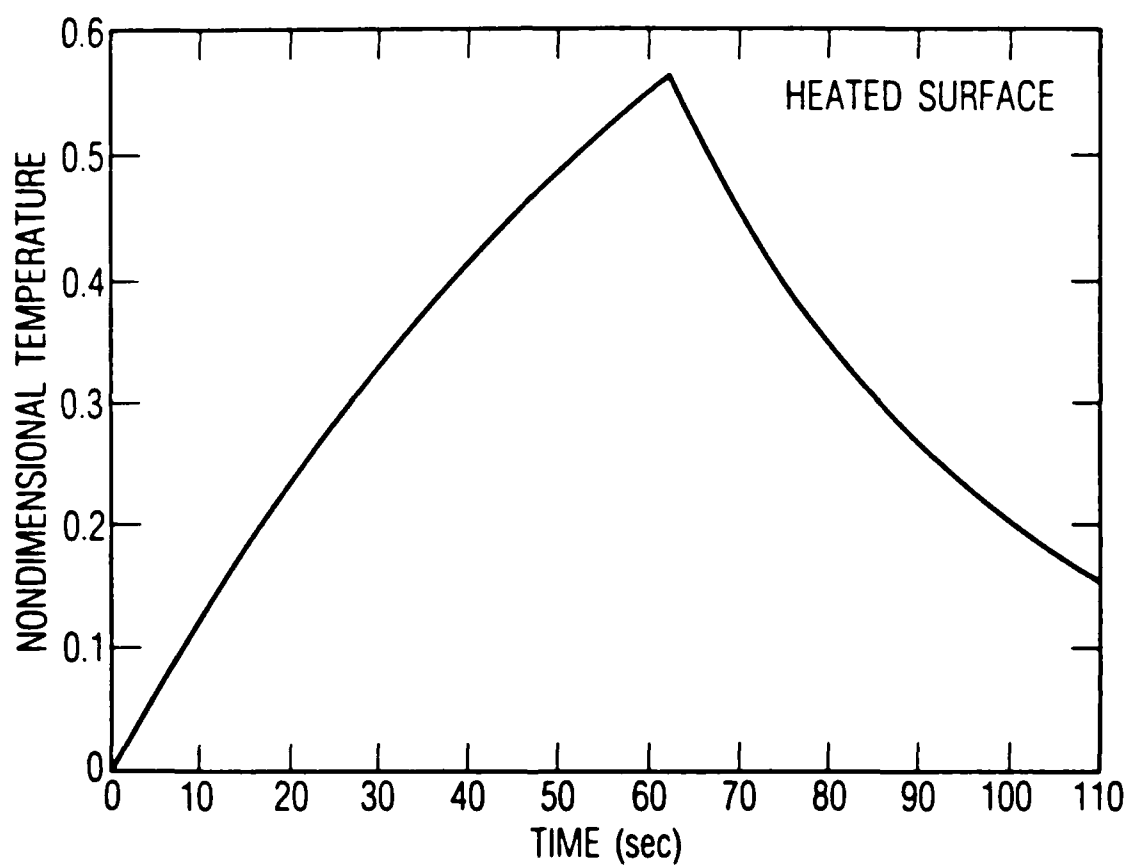


Fig. 2. Nondimensional Temperature History of Substrate

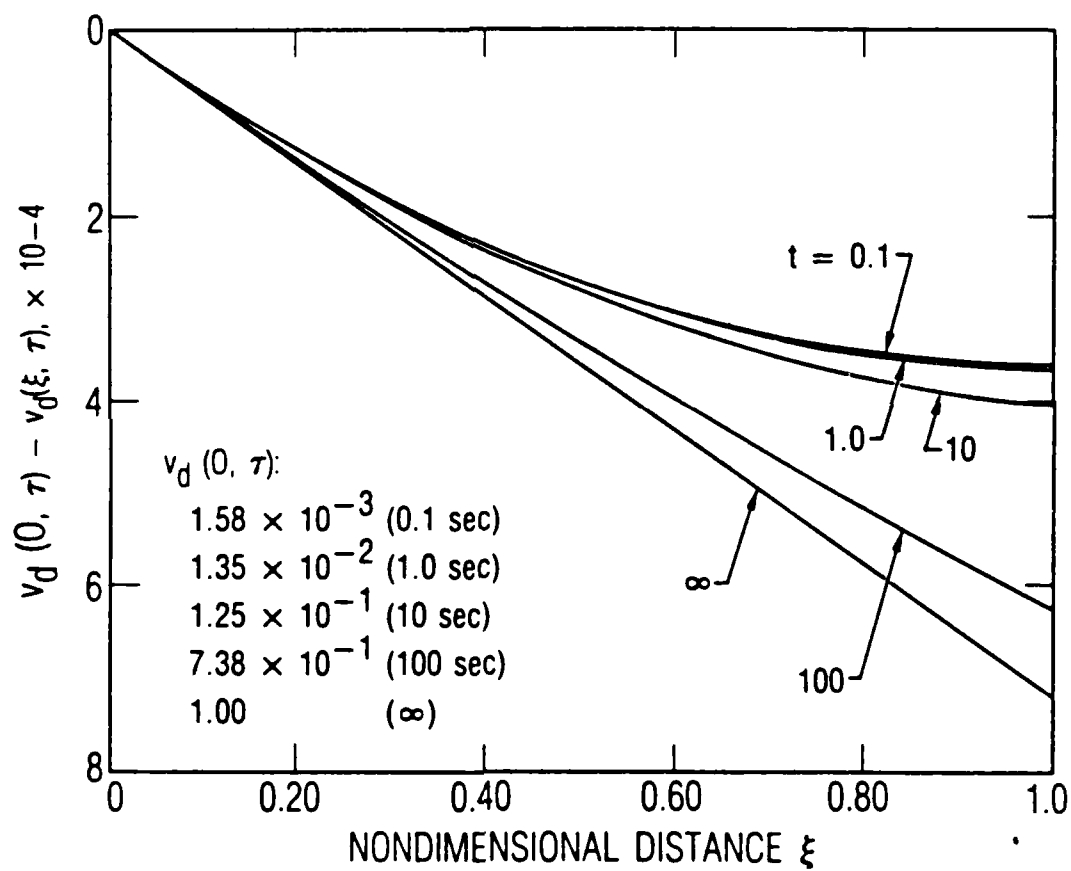


Fig. 3. Nondimensional Temperature During Deposition Across the Substrate for Various Times



The thermal deflection can be predicted once the temperature history in a substrate is determined. To calculate thermal deflection, it is assumed that a circular wafer of radius  $a$ , thickness  $d$ , and coefficient of thermal expansion  $\alpha$ , experiences a temperature variation  $T(z)$  across the thickness over a concentric circular region of radius  $b$ . It is also assumed that the boundary is simply supported. From the known solution,<sup>(7)</sup> the deflection at the center is obtained as

$$w(0) = \frac{6\alpha b^2}{d^3} [1 - (1 + \nu) \log(b/a)] \int_0^d T(z)(z - d/2) dz. \quad (18)$$

The tip deflection,  $\delta$ , of a cantilever plate of length  $l$  with temperature distribution  $T(z)$  across the thickness, is known to be

$$\delta = - \frac{6\alpha l^2}{d^3} \int_0^d T(z)(z - d/2) dz. \quad (19)$$

The integral in Eqs. (18) and (19) can be written in terms of the dimensionless temperature (Eq. 14) as

$$\int_0^d T(z)(z - d/2) dz = (T_1 - T_0) d^2 \int_0^1 v(\xi, \tau)(\xi - 1/2) d\xi. \quad (20)$$

Thermal deflection based on Eq. 20 is shown in Fig. 4; also plotted are the experimental curve for the total deflection by Blackburn and Campbell and the difference, which corresponds to the deflection due to the intrinsic stress. The thermal deflection curve exhibits a sharp initial rise and drop at the end of the deposition period; the corresponding sharp changes in the total deflection curve are displayed in the inset with a magnified scale.

The intrinsic stress-induced deflection curve is smooth and free from sudden rises and drops. It also places the intrinsic stress in tension over the entire time domain. The calculated thermal deflection, based on the temperature gradient of a constant heat flux, predicts a rapid rise at a very short time after the deposition begins. The calculation explains the strange deflection behavior measured and reported by Blackburn and Campbell. A smooth intrinsic-stress-induced deflection-history curve can be obtained by applying

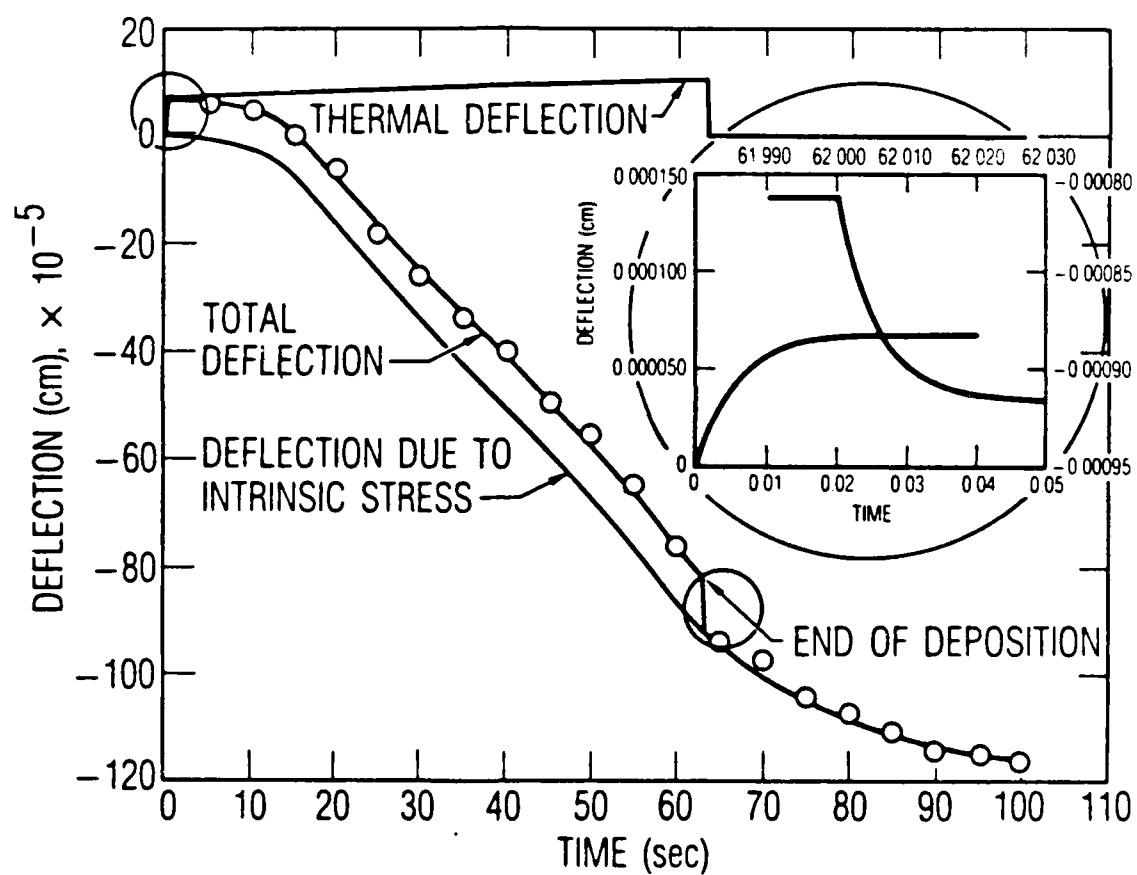


Fig. 4. Deflections Versus Time in Cantilever Substrate

our predicted thermal deflection curve. The final curve not only permits the deflection to approach asymptotically to zero at small time, but also eliminates the sudden deflection drop at the end of deposition. The analytical prediction, together with the observation, strongly suggests that the small temperature difference and yet large thermal gradient between the heated and unheated surfaces cannot be neglected in the deformation calculation for the intrinsic stress determination.

### III. DEVELOPMENT OF DEFORMATION MEASURING TECHNIQUES

The accurate prediction of the intrinsic stress in a thin film relies heavily on the ability to measure the deformation of the system. Therefore, a viable means for in-situ and post-vacuum measurements of the strains must be developed. Furthermore, the technique is also needed in the determination of the material properties which will be discussed later in the section.

The candidate approaches to measuring the displacement of the coating substrate were identified as:

1. Laser interferometry (in-situ, post-vacuum)
2. X-Ray Diffraction (post-vacuum)
3. Differential capacitance (in-situ, post-vacuum)

#### A. LASER INTERFEROMETRY

The Michelson Interferometer (see Fig. 5) consists of a laser source emitting coherent light (indicated by parallel lines in Fig. 5), a beam splitter, a reference flat reflector, a sample substrate, and a photo plate. Light from two separate paths both impinge on the photo plate and create an interference pattern. The first path is from source to beam splitter, where it is reflected to the reference flat and then back through the beam splitter to the photo plate. The second path is from the source through the beam splitter to the sample, where it is reflected back to the beam splitter and then reflected to the photo plate. The nature of the interference pattern is dependent on the difference in path length between the two optical paths. The photo plate is always illuminated uniformly as long as the sample is absolutely perpendicular to the optical axis and the difference between the two path lengths is an integral multiple of the wavelength of the laser light (Fig. 5). If the path length at the sample is changed by one-half wavelength by moving the sample along the optical axis, the photo plate will become uniformly dark because the two light waves will be out of phase and will cancel each other. As the sample is moved along the optical axis, the photo plate will be alternately uniformly bright or uniformly dark depending on whether the two waves reinforce or cancel each other.

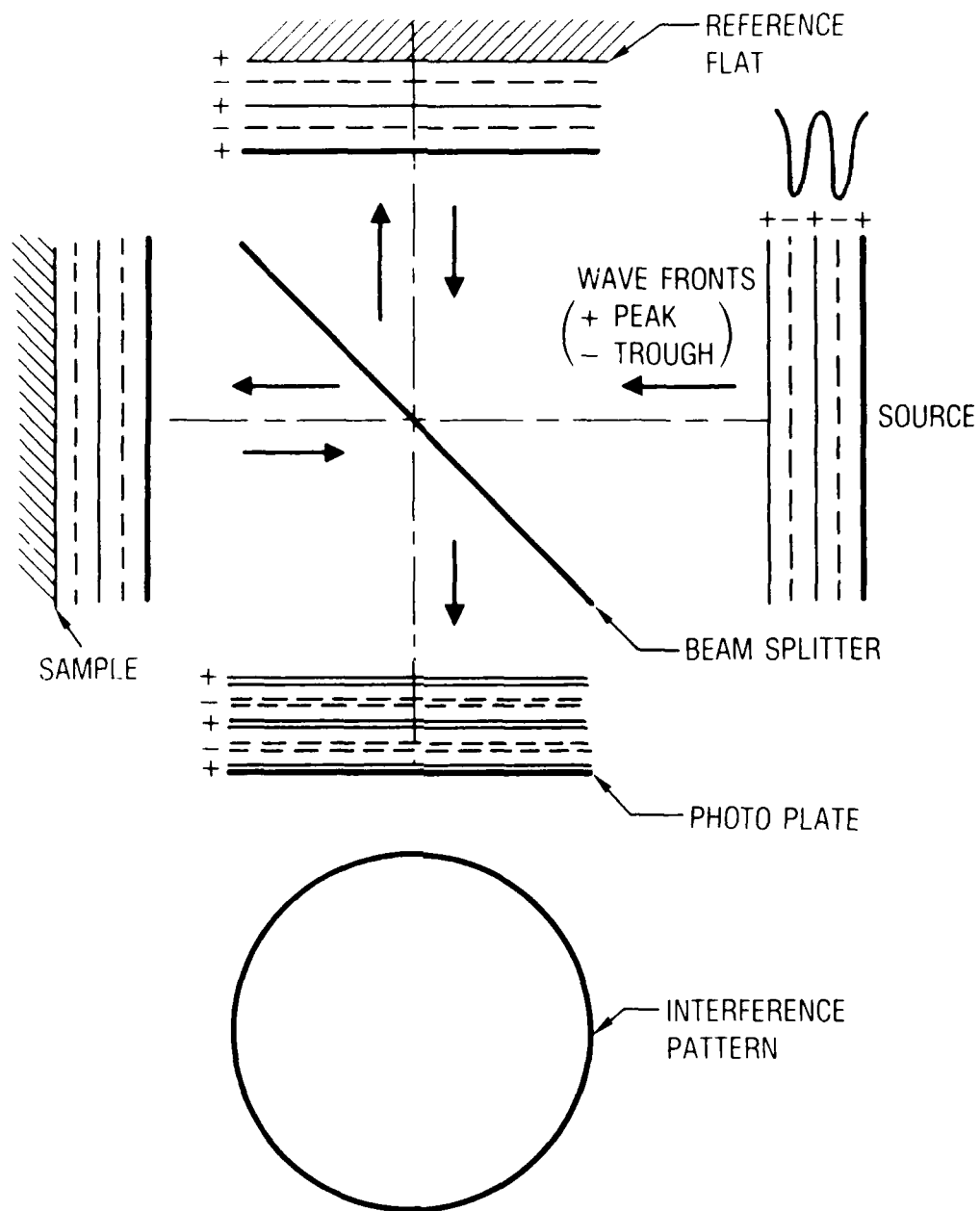


Fig. 5. Michelson Interferometer

Figure 6 illustrates the case where a flat sample is tilted. Dark fringes appear at the photo plate where the peaks (solid lines) interact with the troughs (dotted lines) as the sample beam interferes with the reference beam. The separation between two bright or dark fringes represents one half wavelength of displacement at the sample. (A one-half wavelength displacement causes the optical path length to change by a full wavelength.)

The fringes appear as concentric circles when the sample curvature is spherical (concave or convex) (Fig. 7). To test whether the sample is concave or convex it can be moved slightly towards the source. If the circles expand then the sample is convex. If they contract it is concave.

When a thin film is deposited on a circular substrate, the resulting stress usually causes the substrate to bend spherically, giving a pattern of concentric rings. The important parameter in this case is the displacement, or deflection, at the center relative to the edge. The displacement is measured along the central axis perpendicular to the substrate and is the distance the substrate surface moved as a result of stress in comparison to its pre-stressed condition. This distance can be measured at the photo plate by counting the fringes from the center of the substrate to the edge. The displacement is equal to the number of fringes multiplied by one half the wavelength of the laser light. In actual practice, it is difficult to mount the substrate exactly perpendicular to the optical axis. In this case, where the substrate is at a slight angle, the fringe count from the center to one edge will be different than the count from the center to the opposite edge. A simple correction factor is based on the geometric construction shown in Fig. 8. The corrected displacement is:

$$\delta_c = F_1 - \frac{D_1(F_1 - F_2)}{D_1 + D_2} \quad (21)$$

where

- $F_1$  is the fringe count from center of the ring system to one edge of the coated substrate.
- $F_2$  is the fringe count from the center of the ring system to the opposite edge.

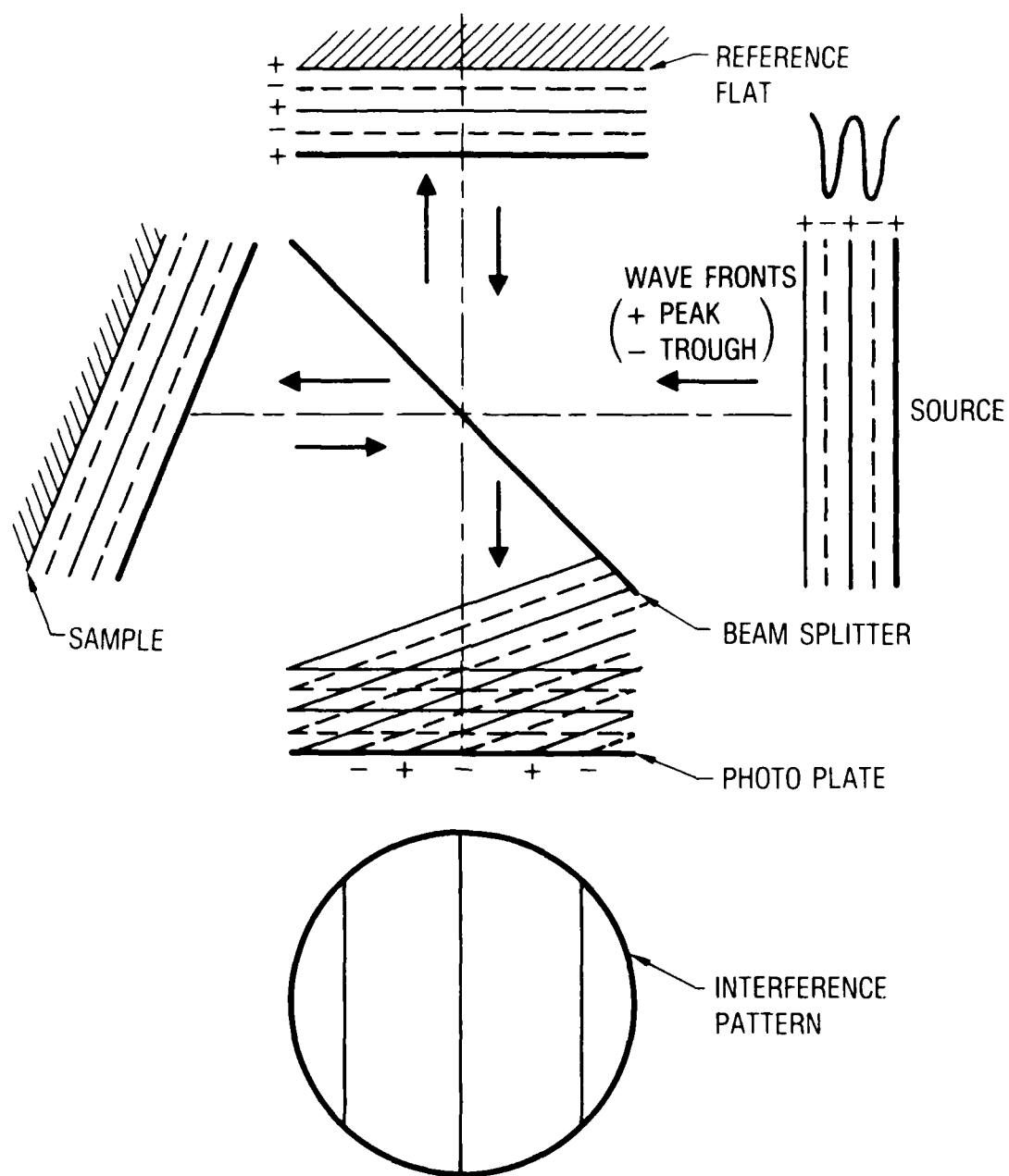


Fig. 6. Tilted Sample

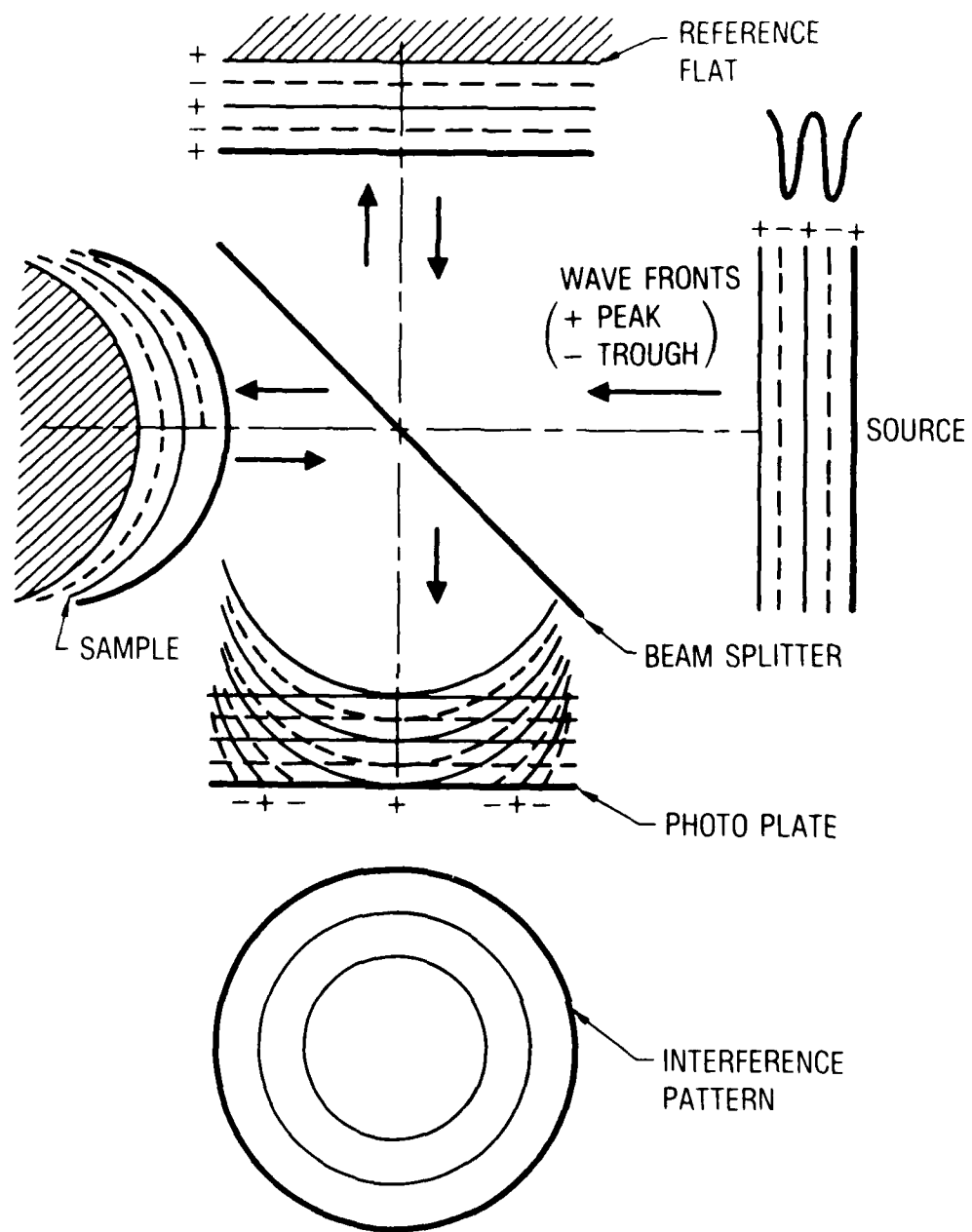


Fig. 7. Spherical Sample



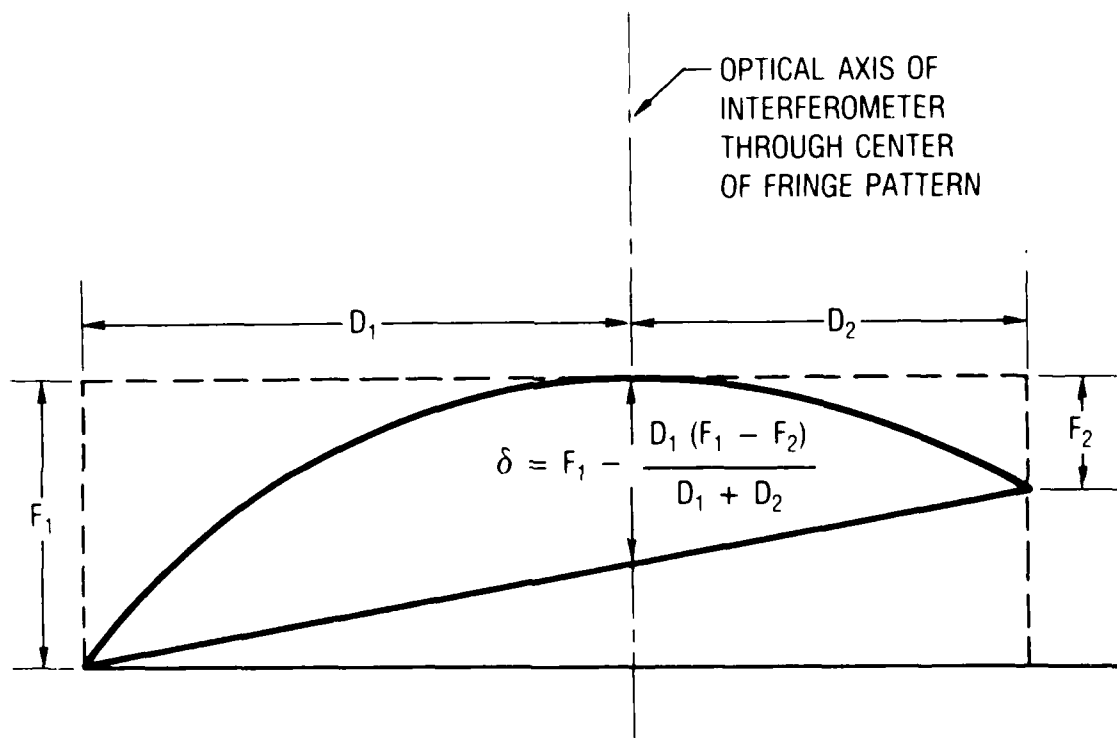


Fig. 8. Tilt Correction

$D_1$  is the distance from the center of the ring system to the same edge used for  $F_1$ .

$D_2$  is the distance from the center of the ring system to the edge for  $F_2$ .

A small part of the outer rim of the substrate is uncoated due to the masking effect of the substrate holder during film deposition. To correct for this condition the following equation is used<sup>(8)</sup>

$$r = r' (1 - \Delta D/D) \quad (\Delta D \ll D) \quad (22)$$

where

$r'$  is the radius of curvature.

$D$  is the diameter of the substrate.

$\Delta D$  is the difference between the substrate diameter and the film diameter.

It is this corrected value for  $r$  that is used in Eq. (3) to calculate the stress.

Additional corrections must be used in cases where the film is thick in comparison to the substrate ( $t > 5\% d$ ). These and other considerations are discussed in Ref. 4.

Initially, a circular wafer was selected as the substrate configuration. A substrate mount was then designed to accommodate a two-inch diameter substrate for both deposition and for pre- and post-deposition assessments. The mount was designed to fit in the sputter deposition chamber, the laser interferometer, and in an x-ray diffraction instrument which was used to obtain additional stress assessment data for correlation.

A general layout diagram of the substrate mount is shown in Fig. 9. The substrate is shown here in a tightly clamped condition with a differential fluid pressure causing it to bow outwards. The ability to exert fluid pressure on the substrate was used to assess the interferometer's ability to measure a small deflection on the substrate. Provision was also made to study

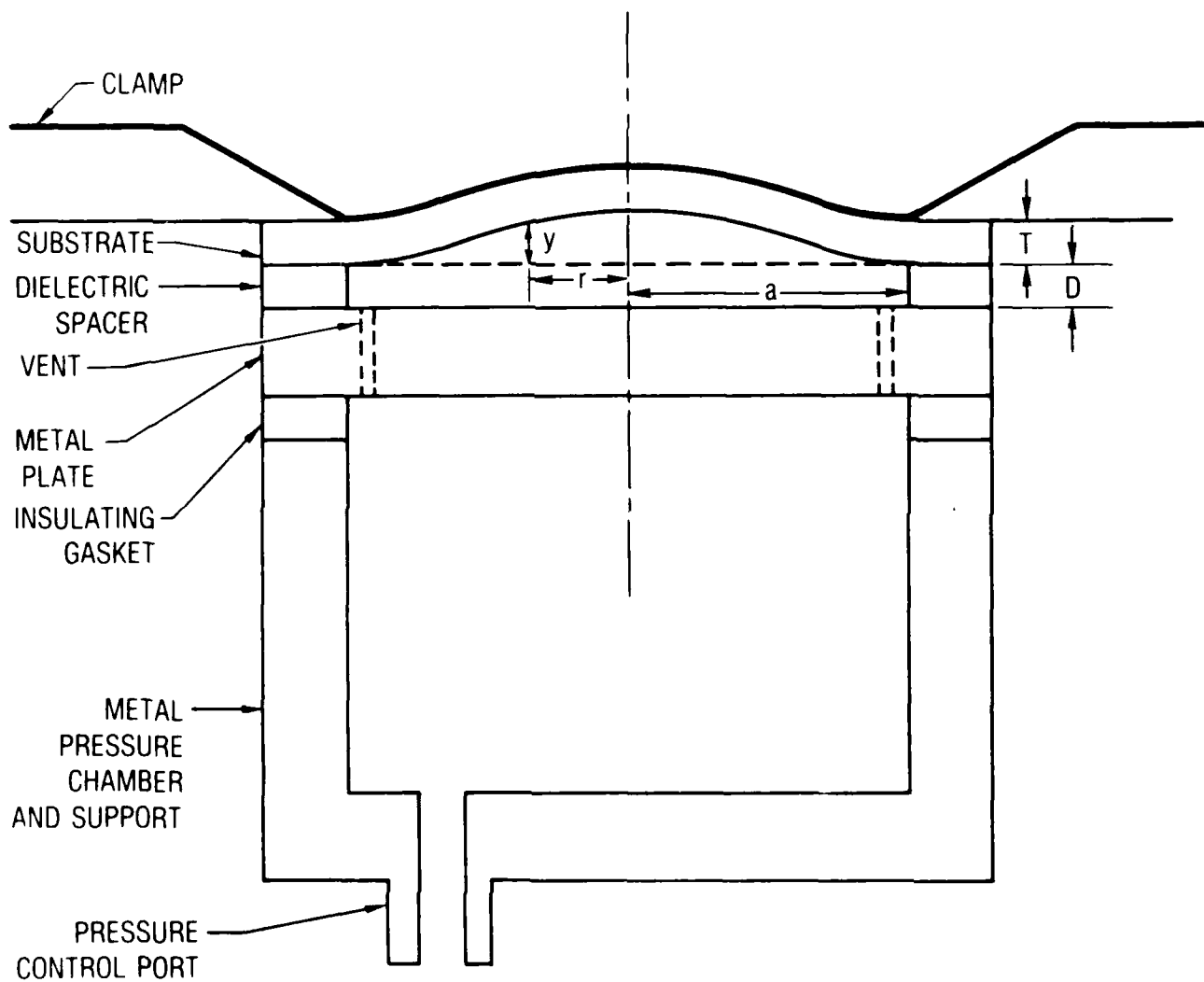


Fig. 9. Substrate Mount

the feasibility of having a capacitance bridge to measure the substrate deflection by using a rigid conducting plate separated from the substrate by a dielectric spacer. Electrical contact to the substrate was accomplished by depositing an aluminum film on the upper surface of the dielectric spacer. The capacitance measurement technique will be discussed in the next section.

An analysis was performed to predict the normal differential pressure versus the maximum deflection relation for a thin circular silicon wafer with a clamped edge. This was done for the purpose of calibrating the laser interferometric measurements. Based on the design, a 5.08 cm (2 in.) diameter silicon wafer is clamped between two stainless steel plates with a 0.238 cm (3/32 in.) wide washer along its edge. The central part of the wafer has a diameter of 2.302 cm (0.90625 in.) and is free to deform under both the external load and residual stress from the coating.

It is known from the strength of materials that the deflection in a flat disk under the action of external load, e.g., residual coating stress or external pressure, depends strongly on the disk thickness and the wafer boundary conditions. When the wafer is circumferentially clamped and is thick, the bending stress dominates in the deflection. The membrane stress becomes more important however, as the wafer thickness is reduced. Therefore, the objective of the analysis was to investigate the deflection sensitivity, and the contribution from membrane and bending stresses of a clamped wafer for various thicknesses and pressure levels.

The equation for determining the pressure exerted on a circular wafer with a clamped edge as a function of maximum wafer deflection is expressed as<sup>(9)</sup>

$$p = \frac{64\lambda}{R^3} \left(\frac{\delta_c}{R}\right) + \frac{8}{3} \frac{E}{(1-\nu)} \frac{t}{R} \left(\frac{\delta_c}{R}\right)^3 \quad (23)$$

where

$p$  = normal differential pressure across the thickness of the wafer

$R$  = radius of the wafer to the clamped edge

E = Young's modulus

$\nu$  = Poisson's ratio

$\lambda$  = plate stiffness, defined as  $Et^3/12(1 - \nu^2)$

The first term on the right hand side of the equation represents the pressure carried by bending action, while the second term represents the pressure carried by membrane action. It can be seen from the above equation that the membrane term becomes large when large deflections, i.e.,  $\delta_c/R$  ratios, prevail. Since it is our goal to ensure that the deflection of coated wafers can be measured with good sensitivity, it would be advantageous to use thin wafers as long as they do not undergo undesirable distortion due to handling.

The pressure was determined as a function of the  $\delta_c/R$  ratio for 0.020 and 0.038 cm (0.008 and 0.015 in.) thick wafers based on a value of 180 GPa for  $E/(1 - \nu)$  and a Poisson's ratio of 0.4 for silicon. The radius was based on the 2.302 cm (0.90625 in.) diameter value.

Figure 10 shows that the bending effect is dominant with a  $\delta_c/R$  ratio of 0.01 or less for a 0.038 cm (0.015 in.) thick wafer. For a  $\delta_c/R$  ratio greater than 0.03, the membrane part controls. They are both significant for  $\delta_c/R$  ratios between 0.01 and 0.03. In the case of a 0.02 cm (0.008) in. thick wafer, the corresponding limiting  $\delta_c/R$  values reduce to 0.005 and 0.02, respectively. Also a thick (0.038 cm) wafer requires a much higher pressure to generate the same deflection as compared to a thin (0.020 cm) wafer. Thus, higher measuring sensitivity is achieved with thin wafers for a given measuring capability.

The original plan was to clamp a substrate in the substrate mount and then perform deposition and stress analysis without removing the substrate from the mount. In this configuration, the thin film must have a smaller radius than the substrate because the bending moment takes place at the edge of the film and there would be no deflection if the edge of the film was at the clamped edge of the substrate. The equation for this configuration is:

$$S = \frac{4\lambda \delta_c}{(1 - \nu_s)r_o^2 \ln \frac{R}{r_o} dt} \quad (24)$$

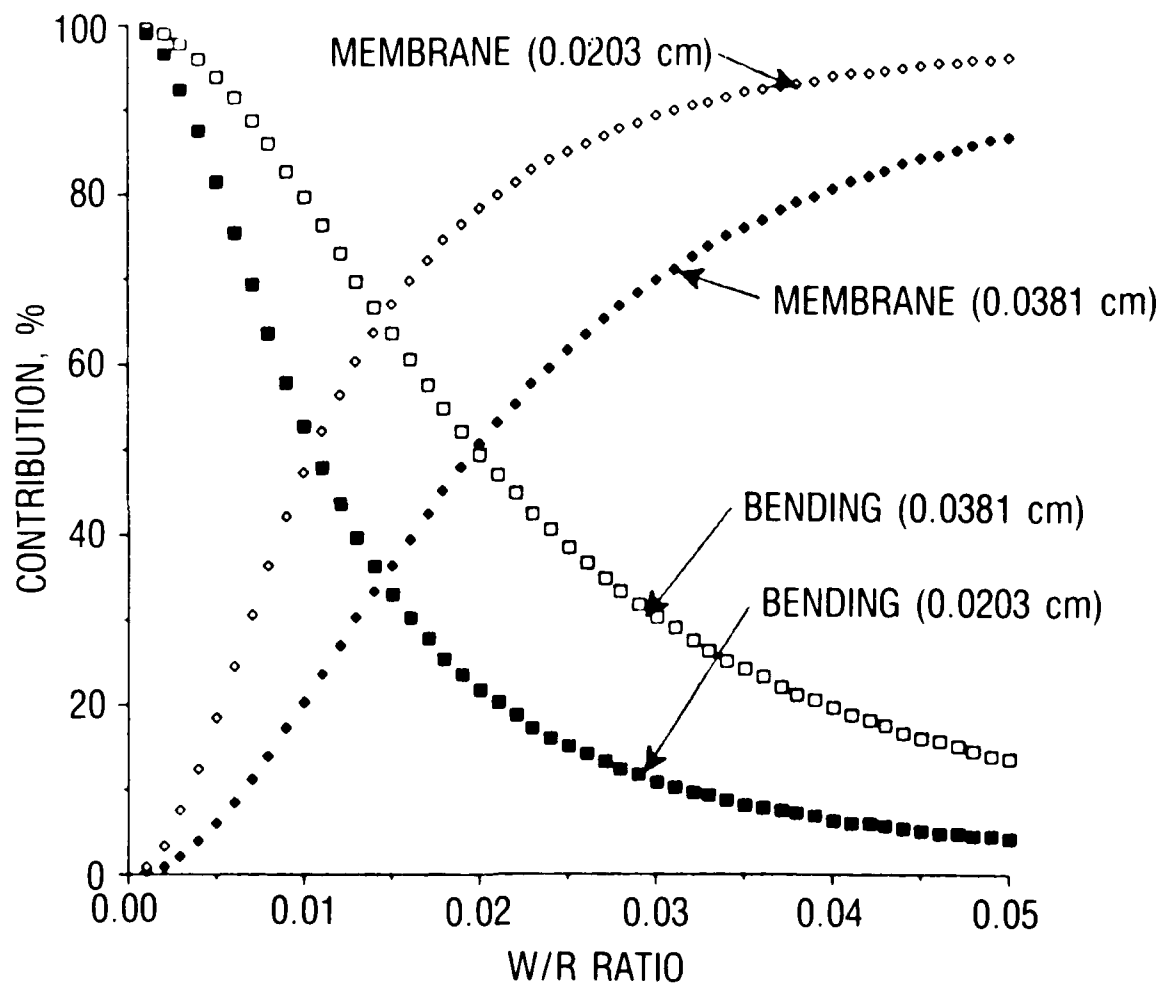


Fig. 10. Normalized Pressure Contribution

where

$R$  = radius of the substrate to the clamp

$r_o$  = radius of the film

$d$  = substrate thickness

$t$  = film thickness

The optimum film radius,  $r_o$ , occurs when  $r_o/R = 1/\sqrt{e}$  where  $e$  is the natural number 2.728, or when the film radius is about .6 of the substrate radius. This method is less sensitive than that of Eq. (3) by a factor of about 6.5, even when the optimum film radius is used.

The deflection vs. pressure of a silicon substrate with a 5.08 cm (2 in.) dia., and 0.028 cm (0.011 in.) thickness was measured by clamping the substrate in the mount and varying the applied air pressure. The air pressure in the mount was varied by means of a bellows type pippette pump and monitored with a glass U-tube manometer containing water. Deflection (from the interferograms) was calculated by using Eq. (22). The data are as follows:

Pressure (inches of water)	Deflection ( $\mu\text{m}$ )	Difference from Zero Pressure ( $\mu\text{m}$ )
+1.0	7.78	-5.56
0.0	13.34	
-1.0	17.95	+4.61

The average displacement, then, for a pressure change of one inch of water was 5.08  $\mu\text{m}$  with an uncertainty of  $\pm .5 \mu\text{m}$  or  $\pm 10\%$ . Note that at zero pressure, there was a displacement of 13.34  $\mu\text{m}$ . This displacement was primarily due to pressure exerted by the clamping ring of the mount.

The expected theoretical center displacement is found to be 4.5  $\mu\text{m}$  for a 5.08 (2 in.) diameter silicon wafer, 0.028 cm (11 mils) thick, ( $E = 11.37 \text{ GPa}$

and  $\nu = .4$ ). The first experimental result, at 2.54 cm (+1.0 in.) of water, was about 21% above the theoretical value, while the result at -2.54 cm (-1.0 in.) of water was close to theoretical. The reason for a higher value at positive pressure is not known at this time. An uncertainty of  $\pm .5 \mu\text{m}$  represents a stress variation of  $\pm 4.12 \times 10^7 \text{ dyne/cm}^2$  for a 0.028 cm thick, 5.08 cm diameter silicon wafer with a  $1 \mu\text{m}$  thick deposited film.

Two thin film coated substrates were evaluated using the interferometer method. One consisted of Ge on a Si wafer and the other was  $\text{Al}_2\text{O}_3$  on Si. Both consisted of  $1 \mu\text{m}$  thick film on 0.028 cm (0.011 in.) wafers. Results were as follows:

Film Type	DEFLECTION OF SUBSTRATE			Stress (Eq. 3) ( $\text{dyne/cm}^2$ )
	Before Deposition ( $\mu\text{m}$ )	After Deposition ( $\mu\text{m}$ )	Difference ( $\mu\text{m}$ )	
Ge	1.58	53.95	52.37	$4.40 \times 10^9$
$\text{Al}_2\text{O}_3$	4.46	20.80	16.34	$1.42 \times 10^9$

The direction of the stress was compressive in both cases. After deposition, the Ge film was etched away in a sulfuric acid bath. The deflection of the substrate was then  $2.06 \mu\text{m}$ . The value agrees with the measurement prior to coating and the deflection measured after deposition was due primarily to thin film stress.

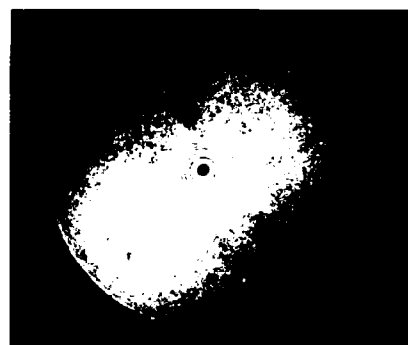
The interferograms made before and after coating the substrate are shown in Fig. 11. As can be seen, the substrates in their original form are not flat but have irregular surface features. The deviation from flatness, however, is small in comparison to the deviation after the coating process. The fringes after coating are so close together towards the edge of the pattern that they merge and cannot be counted on the print. The original



Ge ON Si



PRE-DEPOSITION INTERFEROGRAM



POST-DEPOSITION INTERFEROGRAM

$\text{Al}_2\text{O}_3$  ON Si



PRE-DEPOSITION INTERFEROGRAM



POST-DEPOSITION INTERFEROGRAM

Fig. 11. Interferograms

negative is sharp enough to resolve the fringes right to the edge of the pattern and can be easily counted with the aid of a microscope.

An uncoated substrate was measured before and after heat treatment to determine if there was hysteresis in the amount of deflection. The deflection at the center of the substrate before heat treatment was found, by laser interferometry, to be 22.33  $\mu\text{m}$ . The substrate was then placed in a 900°C oven for 2.5 hours and then cooled to room temperature. The deflection was then measured to be 22.68  $\mu\text{m}$ , indicating negligible temperature hysteresis. The difference, 0.35  $\mu\text{m}$ , is within the experimental accuracy of the interferometer measurement.

An uncoated, but clamped, substrate was tested in the interferometer in a stainless steel mount with an attached thermocouple in order to assess the temperature stability of the system. While periodically recording the fringe pattern, the mount was heated by radiation from a heat lamp and then cooled back to room temperature. No fluid pressure was used. The displacement as a function of temperature is plotted in Fig. 12. The result indicates that the displacement changes with temperature and that this would be a problem for in-situ stress evaluations which are planned as a later phase in this project. The changes in displacement are due to a CTE mismatch between the substrate and its mount. For this reason, a new substrate mount was constructed of Stackpole 2301 CTE graphite which matches the expansion coefficient of silicon very closely.

## B. X-RAY DIFFRACTION

X-ray diffraction (XRD) methods have commonly been used in the measurement of stress in crystalline materials.<sup>(10)</sup> Many of these techniques determine stress by measuring a lattice parameter of a material in several directions. Other XRD methods measure stress in thin films by determining the radius of curvature that a thin film imposes on a single crystal substrate.<sup>(11-14)</sup> Most of these techniques employ the use of a Lang camera or other special instrumentation; however, one method<sup>(14)</sup> makes use of a simple version of a double-crystal diffractometer. Its use for making radius of curvature measurements is simple, provided a double-crystal diffractometer is

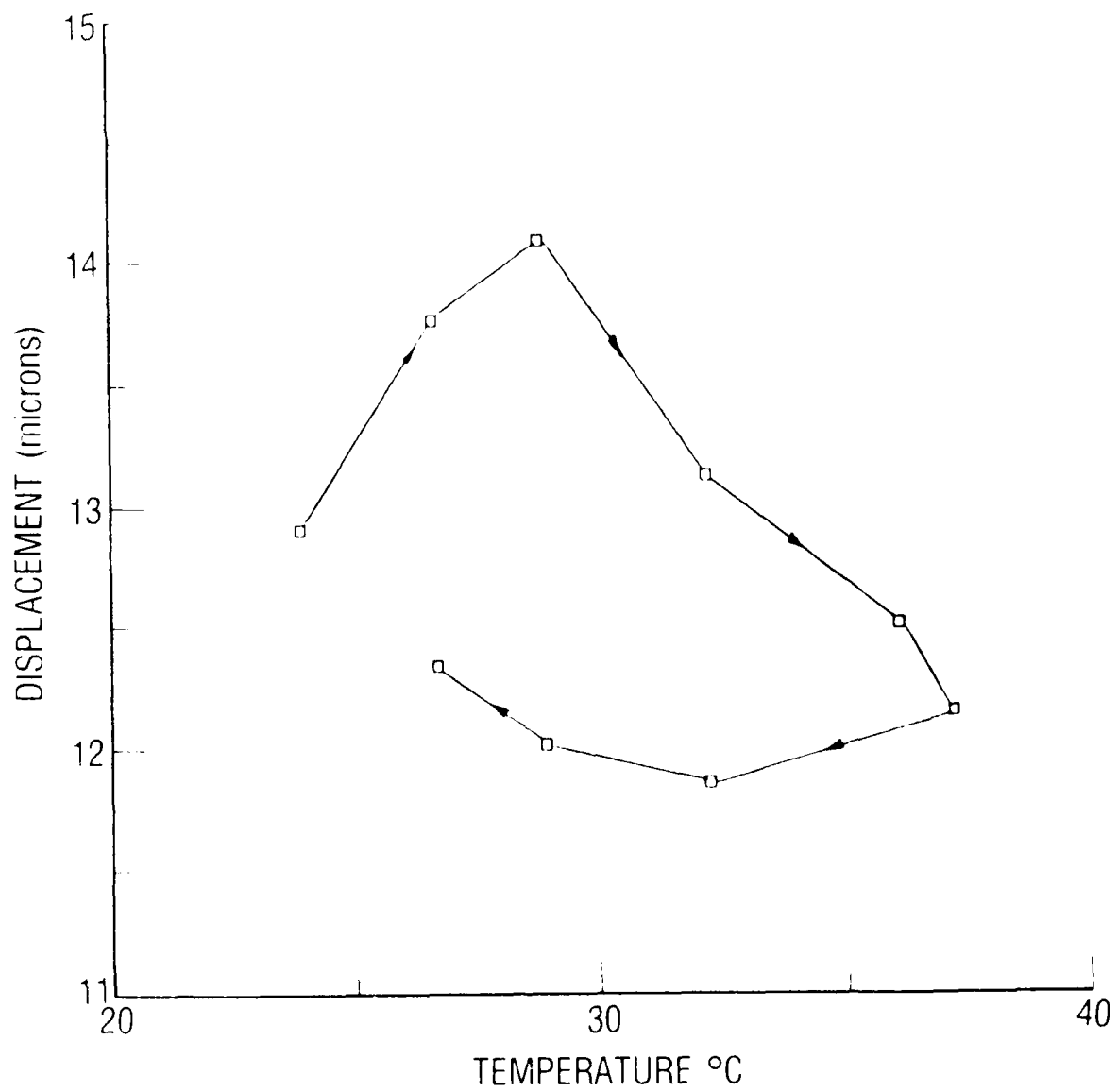


Fig. 12. Displacement Versus Temperature

available. The radii of curvature of several samples were analyzed by the XRD method and were also determined using the laser interferometer. This served as a check on the two methods and provided additional data for evaluation in the selection of a stress measurement method.

Radius of curvature was determined using a modified version of the technique cited in Ref. 11. Measurements were performed on a commercially available (Blake Industries) double-crystal diffractometer using copper radiation and a scintillation detector. The diffractometer was configured in the non-parallel unequispacing asymmetric (+, -) setting (Fig. 13).<sup>(15)</sup> A (100) single crystal silicon wafer was used as a monochromator and was aligned so as to diffract  $\text{CuK}\alpha$  radiation from the (311) lattice planes in the wafer. The purpose for selecting the (311) reflection was to expand the x-ray beam so that it would cover as large an area as possible on the sample. This expansion is possible because one set of (311) planes meets the (100) surface at an angle which is  $2.8^\circ$  less than the Bragg angle ( $\theta$ ). In this configuration, the incident x-rays strike the surface of the monochromator at a very low angle ( $2.8^\circ$ ), in order for diffraction from the (311) planes to occur, and thereby cover a large area.

Samples consisted of 0.028 cm thick 5.08 cm diameter (100) silicon wafers which were aligned to diffract from the (100) planes [(400) reflection]. The sample holder of the diffractometer was modified to accept the specially constructed substrate holder. During initial alignment of the sample, an approximately 3 mm x 3 mm aperture (not shown in Fig. 13) was placed between the monochromator and the sample.

Alignment of the sample consisted of monitoring the intensity of the diffracted beam while the sample was tilted about a horizontal axis and rotated ("rocked") about a vertical axis. The sample tilt was adjusted until it produced the greatest intensity when "rocked". At this point, the normals of the diffracting (311) lattice plane in the monochromator and the (400) lattice planes in the sample are both, as nearly as possible, in the same plane. This will reduce the rocking curve half width of the sample to the

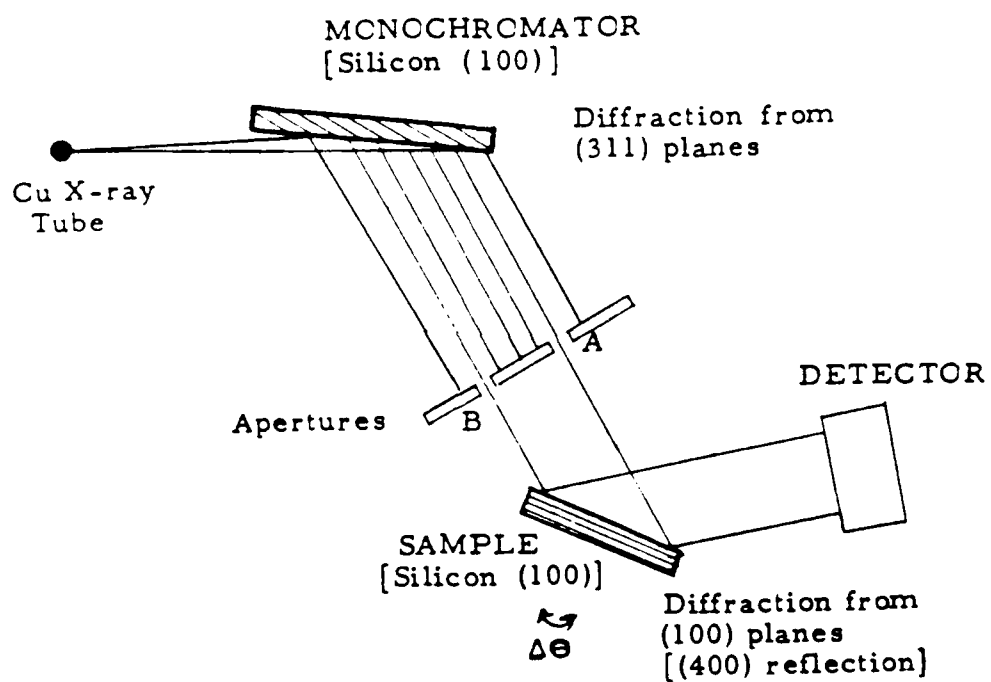


Fig. 13. Diffractometer Setting

point where it is only controlled by the properties of the material and any external strain. Because of the dispersive geometry used in the diffractometer, both the  $K\alpha_1$  and  $K\alpha_2$  reflections will be observed in the rocking curves.<sup>(16)</sup> For the combination of Si (311) and Si (400), the  $K\alpha_1$ - $K\alpha_2$  peak separation (dispersion factor) is 79.8 arc seconds for Cu radiation.

Following sample alignment, rocking curves were recorded with two 1.5 mm diameter apertures placed between the monochromator and sample. The apertures and samples were placed so that the two x-ray beams struck the sample at points on a diameter of the wafer and equidistant from the center ( $\pm 2$  mm). An unstressed wafer will diffract from both beams (A,B) at the same angular position (Fig. 14). In a stressed wafer both beams will not diffract at the same angular position (Fig. 15). The separation of the diffraction peaks from each beam is then a measure of the angular difference between the tangents to the points the two beams strike the sample. A series of rocking curves was run on each sample with aperture spacings (L) of 1.0, 1.4, 1.5 and 1.7 mm. Rocking curves were run with different aperture spacings as a check to see if the wafers were deformed spherically and produced the same radius of curvature independent of aperture spacing. In one instance, rocking curves of a substrate were taken before and after film deposition in order to calculate the stress produced by the film. The sensitivity of the technique is limited by the resolution of the rocking curve and the distance between the apertures.

An analysis was performed to determine the most favorable spacing of two parallel x-rays when the double crystal XRD technique is used. The equation for determining the slope of a thin circumferentially clamped wafer within the small deflection theory, under normal pressure is

$$s = -3pn(1 - \nu^2)(R^2 - \eta^2)/4Et^3 \quad (25)$$

while the equation for the slope difference of two points at a distance L apart along the diametric line can be expressed as

$$ds = -3p(1 - \nu^2) L(3R^2 + 3RL + L^2 - R^2)/4Et^3 \quad (26)$$

SAMPLE: SIDC FILE: SIDCD.SM

11-NOV-85 07:53

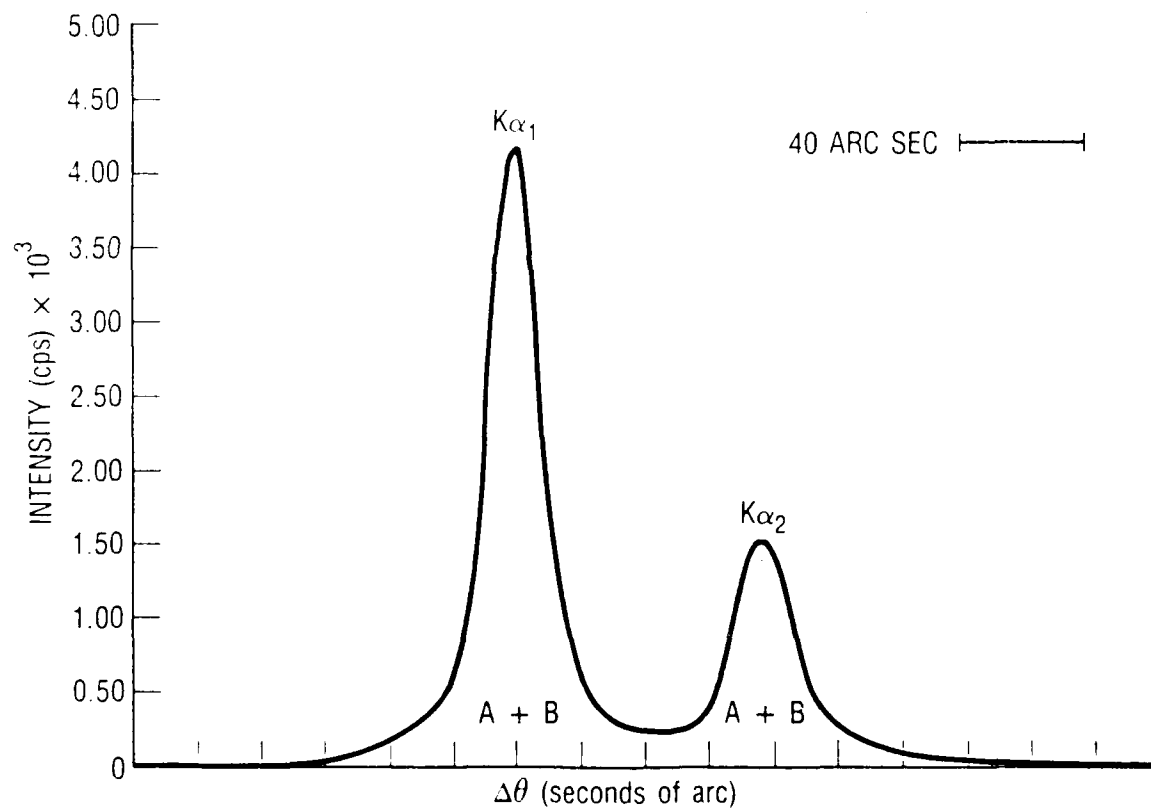


Fig. 14. X-ray Rocking Curve of Unstressed Silicon Wafer

SAMPLE: TST1 FILE: TST10.SM

11-NOV-85 06:58

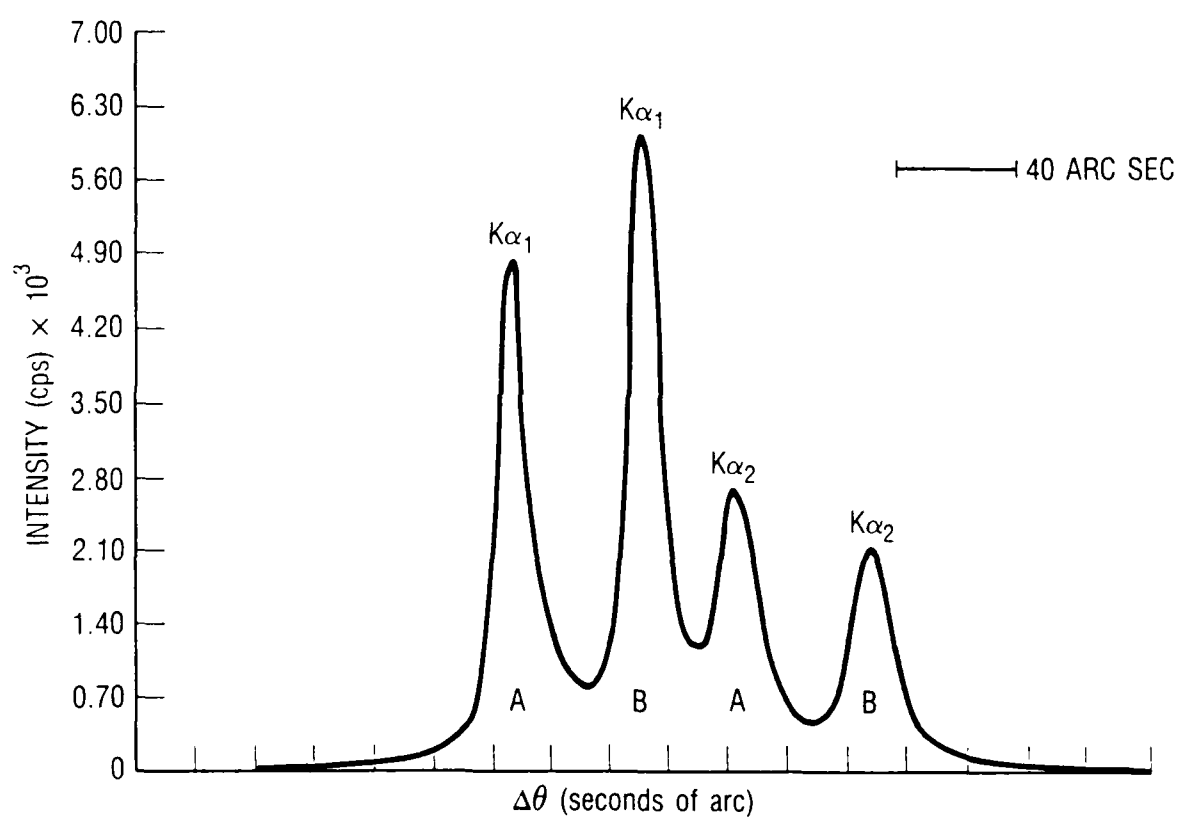


Fig. 15. X-ray Rocking Curve of Sample B,  $L = 1.77$  cm



where

- s = slope
- p = uniformly distributed load intensity
- R = radius of the wafer
- n = radial distance from the center of the wafer
- $\nu$  = Poisson's ratio
- E = Young's modulus
- L = distance between the two fixed x-rays

For this analysis the ratio of  $s/p$  vs.  $r$  was calculated to eliminate the need for a special load intensity. The values used for Young's modulus and Poisson's ratio were that of silicon;  $E = 108 \text{ GPa}$  (15.66 msi) and  $\nu = 0.4$ .

The slope of the wafer as a function of  $r$  is calculated from Eq. (25). A diametric line was used in the calculation because it has the maximum rate of change of slope of any chord on a wafer. The slope difference was obtained by calculating the slopes at the locations of rays 1 and 2 which are at a spacing  $L$  apart (Fig. 16) and then taking the difference of the two slopes Eq. (26). The procedure was performed by first placing two imaginary rays symmetrical about the center of the disk and calculating the slope difference. These imaginary rays were then traversed relative to the wafer by maintaining the spacing distance  $L$ . The slope difference was calculated at an increment of one-fiftieth of the radius until ray 2 reached the disk edge. The clamped wafer was assumed to have an inner radius of 2.302 cm (0.90625 in.) and a thickness of 0.028 cm (0.011 in.) for the analysis. The spacings for  $L$  were 1, 1.7 and 2 cm (0.3937, 0.6693, and 0.7874 in.).

The graphs for the three spacings which were used for the 0.011 in. thick wafer are shown in Figs. 17 through 19. The lower curve in each figure represents the slope along any diametric line as a function of radial distance from center of the wafer. The horizontal coordinate of the slope difference curve measures the location of ray 1 while ray 2 is at a positive distance  $L$  away. In all three cases the maximum slope difference occurs when rays 1 and

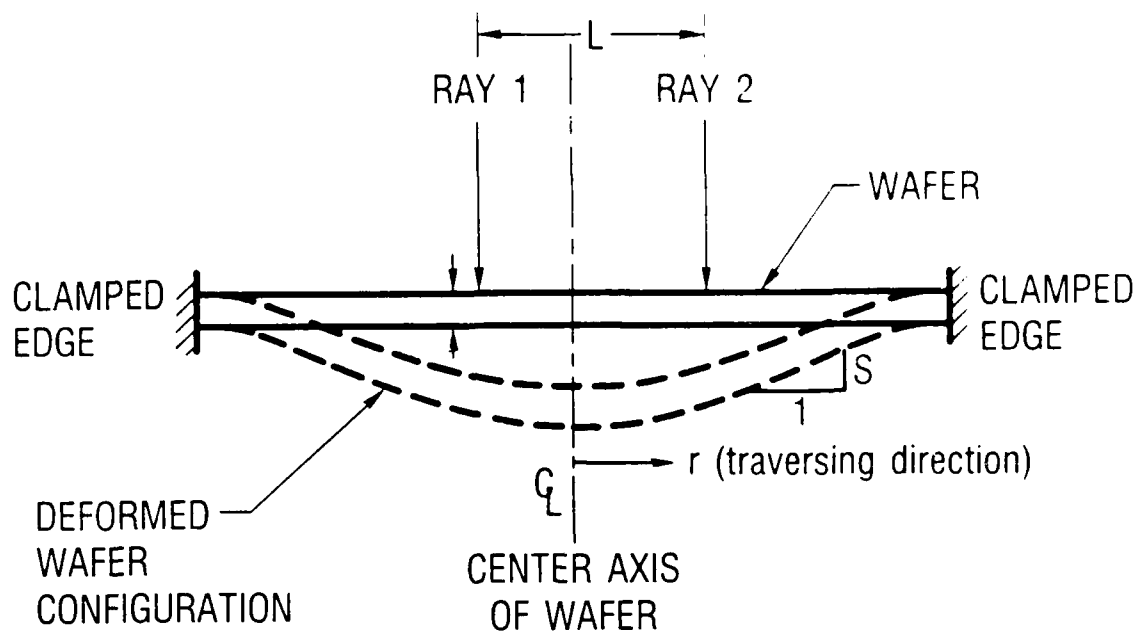


Fig. 16. Schematic of Wafer Configuration

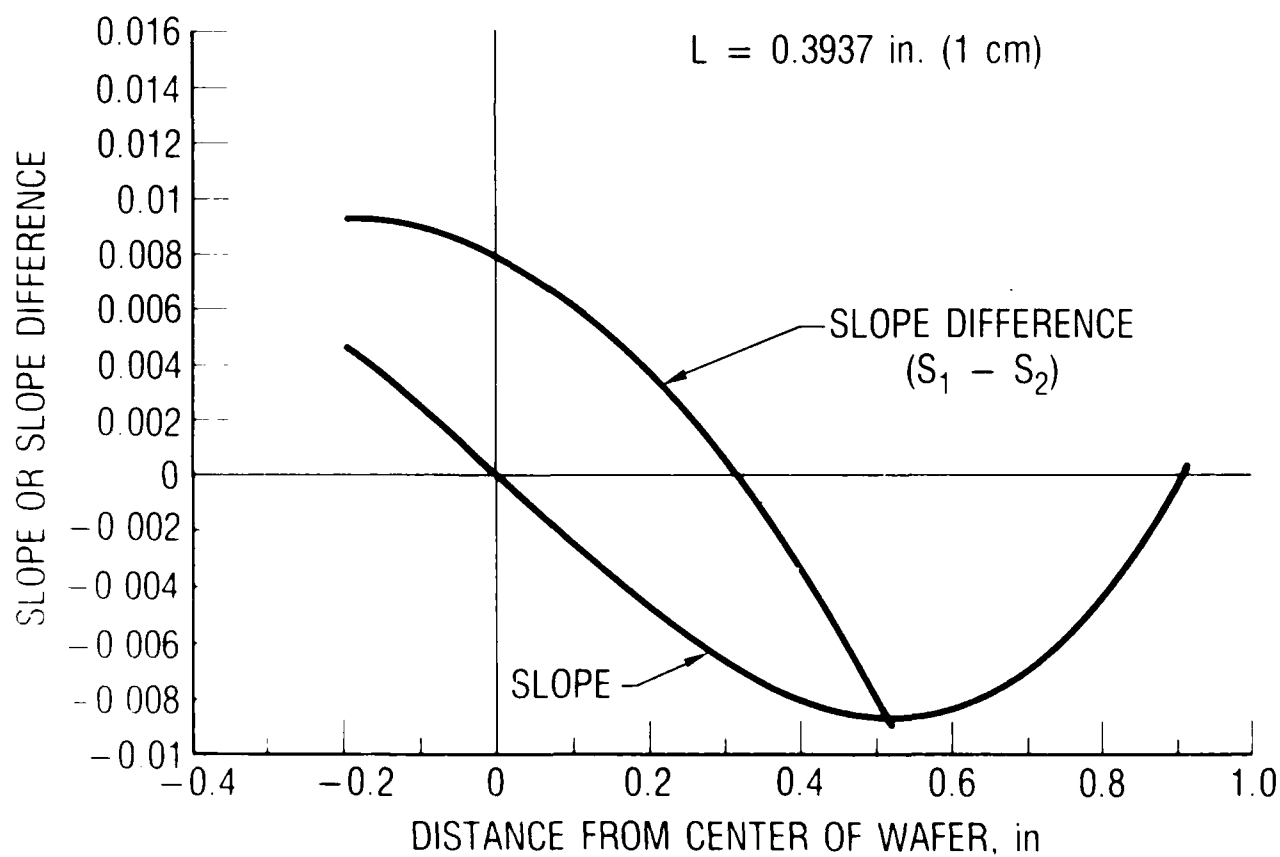


Fig. 17. Slope and Slope Difference of Wafer Versus X-Ray Location for  $L = 1$  cm

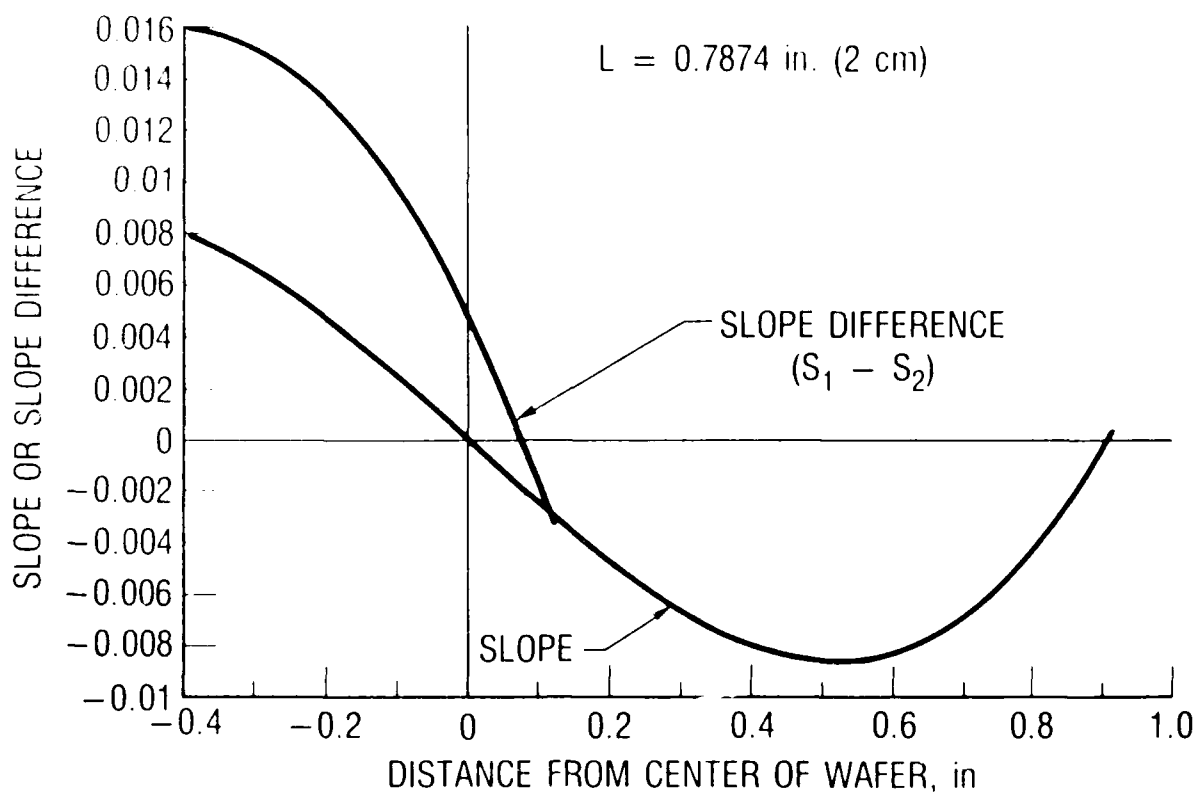


Fig. 18. Slope and Slope Difference of Wafer Versus X-ray Location for  $L = 1.7$  cm

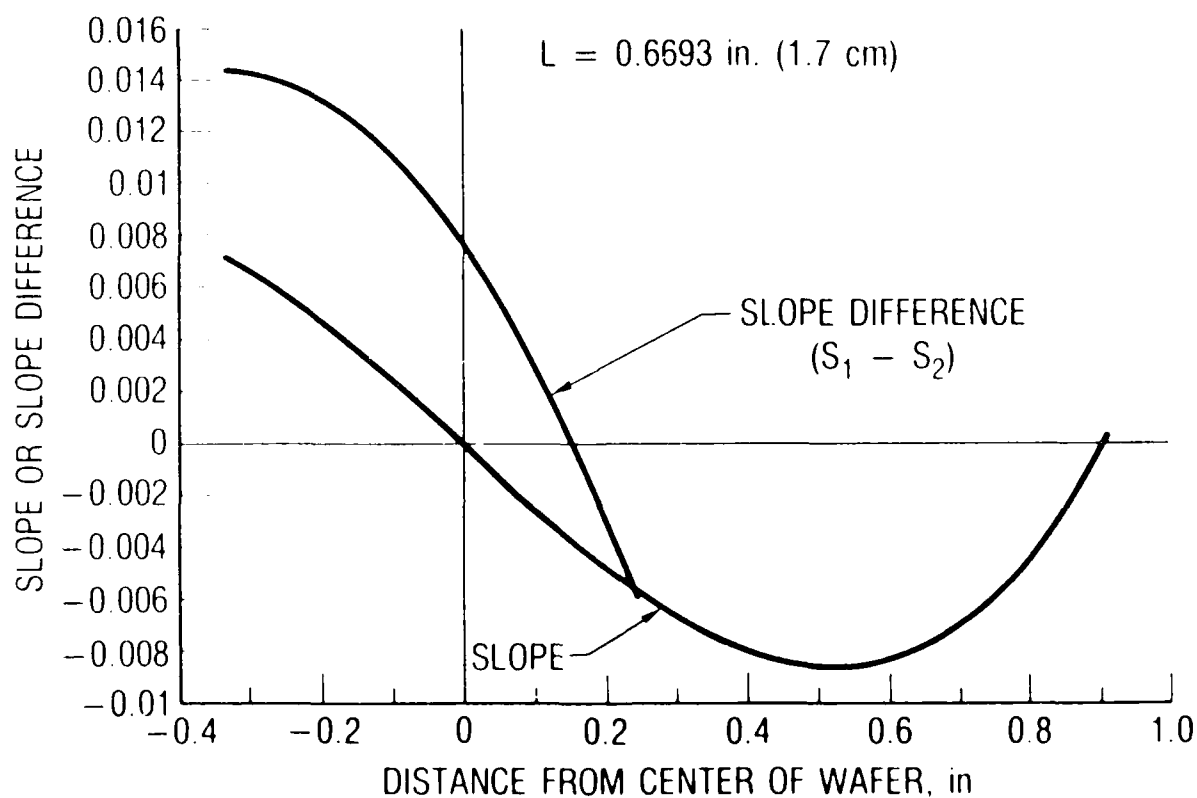


Fig. 19. Slope and Slope Difference of Wafer Versus X-ray Location for  $L = 2$  cm.

2 are symmetrical about the center of the disk. The maximum slope differences are 0.0097, 0.0142, and 0.017 for the three cases (1.0,, 1.7 and 2.0 cm) considered.

The radius of curvature ( $r$ ) for the stress calculation in Eq. (3) is obtained from the relationship

$$r = \frac{L}{\Delta\theta} \quad (27)$$

where

$\Delta\theta$  = the amount of angular rotation between the reflections from the two apertures

$L$  = the distance separating the two x-ray beams on the sample

The direction of the stress can be determined by noting whether the substrate is concave or convex. This is accomplished by alternately blocking one of the apertures and rocking the sample through the x-ray reflection. If the substrate is convex the beam A (reference Fig. 13) will be recorded first as  $\theta$  is decreased. The opposite is true if the substrate is concave.

In calculating the stress in a thin film, the laser interferometer method measures the displacement ( $\delta_c$ ) between the center of the wafer and the edge. To allow comparison with the interferometer method, the quantity  $\delta_c$  is calculated from the radius of curvature, as determined by XRD, with the following expression:

$$\delta_c = \frac{L^2}{8r} \quad (28)$$

The underlying assumption in the XRD method is that the wafer is originally flat, or deformed spherically, and that it deforms spherically as a result of film deposition. This is because the XRD method only measures the angular difference between two points and then calculates  $R$  and  $d$  based on a spherical geometry. It will be shown that this underlying assumption is not always true.

Three as-received wafers (A-C) were analyzed by both the XRD and the laser interferometer methods. An additional wafer (D) which had a strain gauge mounted to its back surface was also analyzed by both techniques, before and after deposition of a sputter deposited Si film. Examples of the XRD rocking curves are given in Figs. 15, 20 and 21. A summary of the XRD and interferometer data is given in Table 3. The data indicates that the as-received silicon wafers are not flat, or that the sample mount may be distorting the wafers, since deformations (in some cases highly non-spherical) are present. This is most easily seen in the interferograms, where concentric equally spaced circular lines would be evidence for spherical deformation.

In some instances (samples A, B) the agreement between the XRD and laser interferometer data is reasonably good ( $\Delta < 10\%$ ) but in other cases (sample D) the differences are as great as a factor of two. Several factors may be responsible for the discrepancies between the XRD and interferometer data. These include:

1. The XRD method assumes that the wafer is spherically deformed, but interferograms suggest that this may not be the case.
2. The locations of where the two x-ray beams strike the sample is assumed to be exactly known, but actually is only known to  $\pm 2$  mm (in both x and y). This would affect the interpretation of the interferograms.
3. The interferograms are also sensitive to non-stress related height differences (wafer or thin film thickness variations) that are interpreted as being a result of stress.
4. In some instances the  $K\alpha_1$  reflection from one x-ray beam may be partially (Fig. 20) or totally superimposed (Fig. 21) on the  $K\alpha_2$  reflection from the other. This may produce a slight peak shift in the observed position of the  $K\alpha_1$  reflection.

The fact that the wafers are not spherically deformed is also indicated by the XRD data since the calculated radius of curvature often varies considerably on a given wafer depending on the separation distance (L) of the two x-ray beams.

The sensitivity of the XRD method is limited by the separation distance (L) of the two x-ray beams on the sample and the resolution of the two diffracted x-ray beams. The aperture of the detector limits L to be no greater

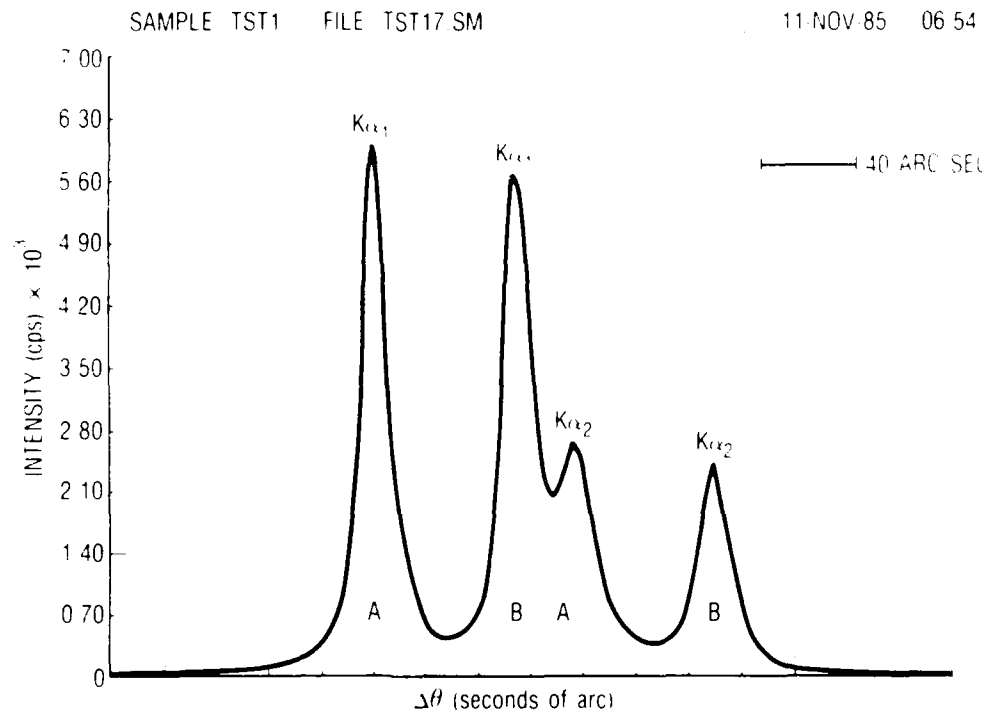


Fig. 20. X-ray Rocking Curve of Sample B,  $L = 3.01$  cm

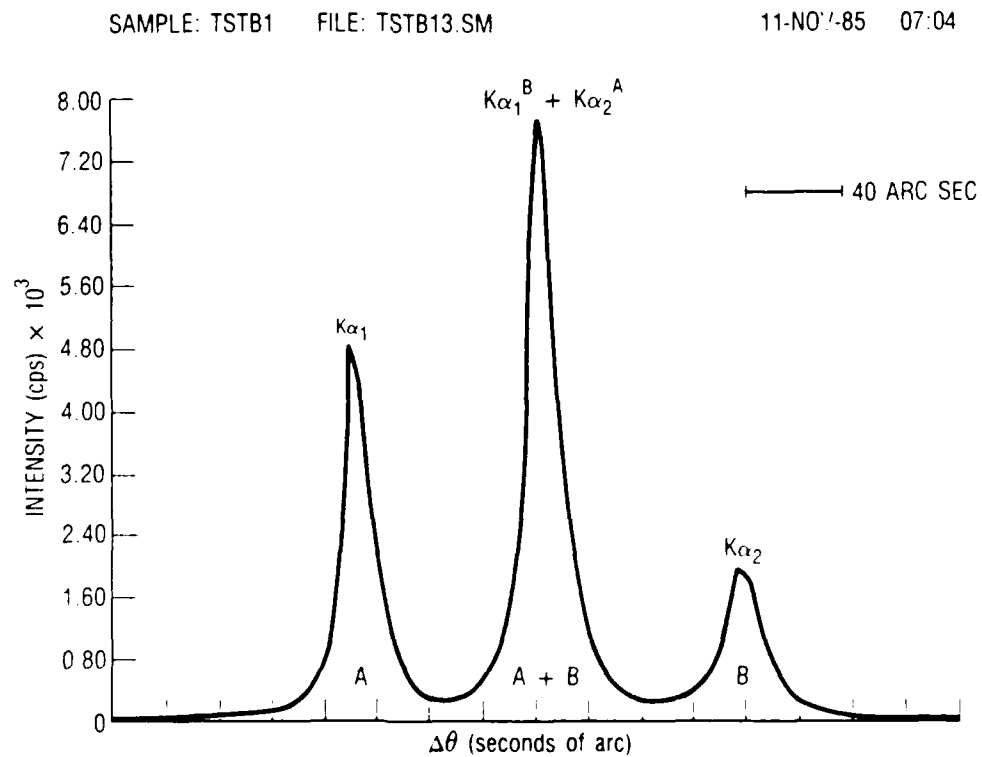


Fig. 21. X-ray Rocking Curve of Sample C,  $L = 2.30$  cm

Table 3. Radius of Curvature and Deflection Data  
Determined from XRD and Laser Interferometry

	X-Ray Diffraction Data				Laser Interferometer Results		
	L (cm)	$\Delta\theta$ ("arc)	Radius of Curvature (m)	$\delta_c^{\#}$ $\delta_c^x$ ( $\mu\text{m}$ )	$\delta_c^x$ ( $\mu\text{m}$ )	$\delta_c^y$ ( $\mu\text{m}$ )	$\delta_c^{\text{ave}}$ ( $\mu\text{m}$ )
<u>Sample A</u>	1.77	139	26.3	1.49	1.90	.79	1.35
(-)*	2.30	147	32.3	2.05	2.37	1.58	1.98
	2.67	166	33.2	2.68	2.78	2.02	2.40
	3.01	188	33.0	3.43	3.05	2.18	2.62
<u>Sample B</u>	1.77	48	76.1	0.51	.32	.79	.56
(-)	2.30	54	87.9	0.75	.63	1.11	.87
	2.67	51	108.0	0.83	.79	2.06	1.43
	3.01	58	107.1	1.06	1.11	3.01	2.06
<u>Sample C</u>	1.77	60	60.9	0.64	1.11	1.74	1.43
(-)	2.30	78	60.8	1.09	1.90	3.16	2.53
	2.67	84	65.6	1.36	2.53	4.43	3.48
	3.01	94	66.1	1.71	3.32	5.22	4.27
<u>Sample D</u>	1.77	263	13.9	2.82	3.64	4.59	4.12
<u>Pre-Film</u>	2.30	286	16.6	3.99	5.70	9.97	7.84
(-)	2.67	316	17.4	5.11	7.44	13.13	10.29
	3.01	347	17.9	6.33	9.02	15.82	12.42
<u>Sample D</u>	1.77	626	5.8	6.72	14.71	12.81	13.76
<u>Post Film</u>	2.30	750	6.3	10.43	22.94	22.94	22.94
(-)	2.67	839	6.6	13.58	29.27	31.64	30.46
	3.01	897	6.9	16.34	35.91	46.04	40.98

\* Sense of Stress

- = compressive

+ = tensile

# = See Figure 22 for coordinate system.

than 3.01 cm and the resolution of the rocking curves is on the order of 5 arc seconds. The largest detectable radius of curvature is then approximately 1240 m. For a film thickness ( $t$ ) of 0.10  $\mu\text{m}$  and a radius of curvature ( $r$ ) of 1240 m, the smallest measurable displacement ( $\delta_c$ ) is 280  $\mu\text{m}$  and since for {100} Si:

$$\frac{E_s}{(1 - \nu_s)} = 1.805 \times 10^{12} \text{ dynes/cm}^2 \text{ (Ref. 13)}$$

Then, from Eq. (1) and the above stated conditions, the minimum detectable thin film stress  $S = 1.89 \times 10^8 \text{ dynes/cm}^2$ . This compares with a value of  $6 \times 10^7 \text{ dynes/cm}^2$  reported in Ref. 14 using Fe radiation and the (440) reflection. It is to be noted that the non-spherical deformation places a limitation on the XRD method of stress measurement, since it calculates the radius of curvature ( $r$ ) and the displacement ( $\delta_c$ ) based on a spherical geometry. A further limitation with the double-crystal XRD method of stress measurement is its dependence on single crystal substrates. This would eliminate it from consideration with polycrystalline or amorphous substrates which are planned for future use in the program.

### C. DIFFERENTIAL CAPACITANCE

It has been demonstrated experimentally that laser interferometry can be successfully used to characterize the flatness of pre-deposited wafers and the deformation of post-deposited wafers. The sensitivity of the displacement measurement depends upon the wavelength of the laser. However, if the in-situ deformation is desired during the coating deposition, problems are expected due to the difficulty of setting the light path and the vibrational motion of the sputtering system. It was determined after a careful study that laser interferometry may not be feasible for the in-situ deformation measurement. The double-crystal XRD technique is also applicable for post deposition deformation measurement. Like the laser interferometer, the vibrational motion, together with the bulky apparatus, make the measurement impractical. In addition, the in-house XRD equipment cannot be used on polycrystalline or amorphous structures.



The differential capacitance method has been used as a viable way to measure deflection of structures. It works on the principle that the electrical capacitance between two conductor plates separated by an insulator is linearly inversely proportional to the distance between the two plates. From past experience, a change of dimension  $\Delta d$  between two capacitance plates, which are at a distance  $d$  apart, can be measured to  $10^{-5} d$  by the use of the equation:

$$\Delta d = \frac{\Delta C}{C} d \quad (29)$$

when  $C$  is in the range of 10 pF. Therefore, a deflection sensitivity of 0.13  $\mu\text{m}$  (5.0  $\mu\text{in.}$ ) can be achieved if the initial gage distance between the two plates is no more than 0.013 cm (0.005 in.). The normal deflection of an edge-clamped circular wafer under the application of normal pressure can be measured by the use of the differential capacitance method by measuring the capacitance between the substrate and a rigid metal plate. The differential change in capacitance as a function of pressure is given by Neubert as:

$$\Delta C = .0174 \frac{K(1 - \nu^2) R^6}{E d^2 t^3} p \quad (30)$$

where  $p$ ,  $R$ ,  $t$  are the applied pressure, radius and thickness of the plates, respectively, and  $d$  is the distance between the plates. The initial capacitance is that of a pair of circular plates separated by a dielectric:

$$C = \frac{KA}{3.6 \pi d} = \frac{KR^2}{3.6 d} \quad (31)$$

where  $A$  is the area of the circular plate. The fractional change of capacity as a function of pressure is then:

$$\Delta C/C = 0.0625 \frac{(1 - \nu^2) R^4}{E d t^3} p \quad (32)$$

Combining Eq. (30) with Eq. (23), neglecting large deflection effects, we get:

$$\delta_c = 3d \Delta C/C \quad (33)$$

The capacitance between the Si substrate and the fixed metal plate was measured by means of an impedance analyzer (Hewlett Packard Type 4191). The air pressure in the substrate mount was controlled and monitored as it was for the deflection vs. pressure experiment. A test frequency of 4 MHz was used in the impedance analyzer. Capacity resolution was about  $\pm .2$  pF. The total measured capacity was made up of the following components:

1. Substrate initial capacity (inside clamp)	117.7 pF
2. Capacity of clamp ring	77.0
3. Capacity of connecting cable	<u>91.9</u>

Total capacity 286.6 pF

A comparison of the MSL measured capacitance values to the calculated values based on Eq. (3) is shown below.

Pressure (inches of water)	Capacity (pF)	Change From 286.6 (pF)	Change Per Inch of Water (pF)	Deviation From Theoretical 1.415 (pF)/ in. of water
+1	285.1	-1.5	1.5	+6.0%
-1	287.8	+1.2	1.2	-15.2
+2	283.9	-2.7	1.35	-4.6
-2	289.3	+2.7	1.35	-4.6
+3	282.5	-4.1	1.37	-3.2
-3	290.9	+4.3	1.43	+1.1
+4	281.0	-5.6	1.40	+1.1
-4	292.8	+6.2	1.55	+9.5

By Eq. (33), the deflection due to  $\pm .2$  pF (the approximate uncertainty of the above data) is calculated to be  $\pm .65$   $\mu\text{m}$ . The equivalent stress (assuming a one micron deposited film) is  $\pm 3.86 \times 10^8$  dyne/cm<sup>2</sup> (5600 psi). This represents the uncertainty of the capacitive method with a clamped substrate. The  $\pm .65$   $\mu\text{m}$  uncertainty of measured deflection is not much worse than the  $\pm .5$   $\mu\text{m}$  uncertainty of the interferometry method (Appendix B, page B-1), but an unclamped substrate can be used when the interferometry method is used for stress measurements, giving an order of magnitude improvement of stress sensitivity.

In-situ test runs were made to measure the deflection of Si wafer substrates during coating deposition. It was observed that RF signal interference was not a problem during the entire course of the data acquisition. Also, the vibrational motion of the sputtering system did not affect the measurement since the capacitance device was an integral part of the specimen/holder assembly. Consequently, it has been concluded that the differential capacitance method is the best among all three techniques in the measurement of substrate deformation for pre, in-situ, and post-deposition configurations. Test runs were made for bare wafers and post-deposition wafers with 4  $\mu\text{m}$  thick Si/Ge discrete and rugate coatings. Table 4 illustrates the comparison between the laser interferometry and the differential capacitance methods. It is seen that the results of using two methods differ by 30 - 40%, which might be caused by possible sample movement as a result of sample holder handling.

A concern was raised regarding the actual boundary (edge) behavior of a circular wafer in the sample holder. It has been predicted analytically that the maximum center deflection of a simply supported circular plate under normal pressure is about four times as large as that when it is clamped along its edge. Since the former case has better deflection sensitivity, the edge was only "finger tight" in the actual assembly to provide the best possible simply supported boundary condition while still minimizing possible non-stressed related movement. However, the "finger tight" boundary condition will not eliminate possible specimen movement.

Table 4. Comparison Between Laser Interferometry and Capacitance Methods

Wafer: 110 Mil Thick, 2" Diameter Si  
Coating: 4  $\mu$ m Thick Si/Ge

Measurement Instrument	Type of Coating	Maximum Displacement Difference ( $\mu$ m)	Predicted Residual Stress (Dyn/cm <sup>2</sup> )
Laser Interferometry	Discrete	8.47	$5.70 \times 10^8$
	Rugate	9.23	$5.20 \times 10^8$
Capacitance	Discrete	11.01	$7.40 \times 10^8$
	Rugate	13.20	$8.88 \times 10^8$

It was found during the calibration runs of the capacitance instrumentation that reasonable data were obtained when the wafer was placed horizontally with no clamping force from the holder and with only gravitational force exerting downward. However, when the wafer specimen is placed vertically in the holder, there needs to be some clamping force (e.g., finger tight) from the holder. The magnitude of this force cannot be measured. Also, there might be a small gap existing between the wafer and the holder in some places. Consequently, no reliable deflection data could be obtained.

After reviewing the other supporting methods and considering that high deformation sensitivity is vitally important, it was decided that the cantilever method, rather than the circular wafer method, should be used to measure substrate deflection. The decision was based upon the following observations:

1. The tip-deflection of a cantilever, as shown by Eq. (6), due to film-stress is 4 times the central deflection of a simply supported circular wafer if every condition is the same and the length of the cantilever is equal to the diameter of the wafer.

2. The specimens used for in-situ measurement need to be placed vertically. The cantilever can be clamped without any difficulty, while the simply supported condition for the wafer is very difficult to achieve in the vertical position.
3. Most of the published data on film-stress have been obtained by the cantilever method.
4. Analytical expressions of the physical quantities are much simpler and more compact for the cantilever than for the circular wafer.
5. Some improvements on the cantilever method have been proposed, but improvements to the circular wafer method seem to be difficult.

A new sample holder and specimens have been fabricated for the cantilever configuration. More calibration runs for bare and thin-film deposited specimens will be performed.

#### IV. MATERIAL PROPERTY DETERMINATION

In the assessment of the stress response in the coating for a thin-film deposited substrate, the material properties for thin-film materials, e.g., Young's modulus, shear modulus, coefficient of thermal expansion, need to be determined. Unfortunately, the properties of thin-film materials are not necessarily the same as the bulk materials.<sup>(17)</sup> Also, the different coating techniques, e.g., evaporated, electroplated, and chemically deposited coatings yield different properties. Therefore, an accurate prediction of the film stresses under operational environments is contingent on reliable property input for the coating materials.

Because of the very thin character of thin-film coatings (4000 Å or less), the measurement of their Young's moduli cannot be achieved by the use of conventional methods. Some measurements have been done by other investigators using the bulging of a coating from an applied normal pressure to the coating when part of the substrate was etched away. This is valid only if the moduli of coatings are not a strong function of the intrinsic stresses. When the properties change with respect to the existing intrinsic stress, other techniques need to be explored.

Cantilever reeds or strips are being used for the substrate configuration for the material property measurement. The coatings will be deposited with controlled parameters such as temperature, deposition rate and total thickness.

##### A. DETERMINATION OF YOUNG'S MODULUS

The fundamental bending frequencies of the specimen before and after the deposition will be measured. Due to the film deposition, the added coating affects the fundamental frequency of the cantilever substrate. Since the coating is an integral part of the cantilever substrate, Young's modulus of the coating materials can be expressed in terms of frequency change and other specimen and material parameters.

It is realized that intrinsic stresses develop as a result of coating deposition. The magnitudes of the intrinsic stresses may be large enough to cause yielding in the coating. Therefore, it is possible that the tangent modulus at the stress level differs from the initial tangent modulus (Young's modulus) of the material. One may thus expect that the measured modulus using a vibration cantilever will not give the Young's modulus value. In fact, when the specimen is vibrated, the stress in the coating will increase first to its maximum value and then decrease during the first cycle. Although it may follow the nonlinear part of the stress-strain curve during initial loading, the linear unloading stress-strain curve will be followed in the subsequent cycles. If no fatigue damage is assumed to occur from the vibration, the Young's modulus of the coating is expected to be obtained from the vibration technique.

The basic equation for the fundamental frequency of a uniform cross sectioned cantilever strip is furnished in Ref. 18,

$$f_0 = \frac{\alpha_0^2 d_s}{4\pi l^2} \left( \frac{E_s}{3\rho_s} \right)^{1/2} \quad (34)$$

where  $E_s$ ,  $\rho_s$ , and  $d_s$  are Young's modulus, density and thickness of the substrate, respectively,  $l$  is the unsupported length of the cantilever and  $\alpha_0$  is a constant ( $\alpha_0 = 1.8751$ ). As the film is deposited onto the substrate, the fundamental frequency  $f_0$  shifts to  $f$  according to

$$f = \frac{\alpha_0^2}{2\pi l^2} \left( \frac{A}{\rho_s d_s + \rho_f d_f} \right)^{1/2} \quad (35)$$

where

$$A = \{d_s^3 E_s + d_f^3 E_f + 3d_f d_s (d_s + d_f)^2 E_s E_f / (d_s E_s + d_f E_f)\} / 12$$

and

$\rho_f$  = density of the film

$d_f$  = thickness of the film

$E_f$  = Young's modulus of the film

The vibrating reed method has been successfully employed to determine Young's moduli of thin films coated on substrates<sup>(18)</sup> and to study the adherent characters of the coated film.<sup>(19)</sup> This method does not require the separation of the film from the substrate and is especially useful for determining the moduli of materials that are stable only in the form of the films on a substrate. Rugate films containing amorphous Germanium are known to be stable only in the coated form.<sup>(20)</sup>

To determine Young's modulus of the deposited coating, a good understanding of the fundamental frequency change versus the ratios of density and thickness of the two materials (substrate and coating) is important. Therefore, an assessment of the sensitivity of  $E_f/E_s$  vs.  $\rho_f/\rho_s$ ,  $d_f/d_s$ , and  $\Delta f/f_0$  is needed for the successful prediction of the coating modulus.

Given a coating thickness such that  $d_f/d_s \ll 1$ , Eq. (35) reduces to

$$f = f_0 \left\{ 1 + a \frac{d_f}{d_s} + b \left( \frac{d_f}{d_s} \right)^2 \right\} \quad (36)$$

where

$$a = \frac{3}{2} \left( \frac{E_f}{E_s} \right) - \frac{1}{2} \left( \frac{\rho_f}{\rho_s} \right)$$

and

$$b = \left[ 3 - \frac{3}{4} \left( \frac{\rho_f}{\rho_s} \right) \right] \left( \frac{E_f}{E_s} \right) - \left( \frac{21}{8} \right) \left( \frac{E_f}{E_s} \right)^2 + \frac{3}{8} \left( \frac{\rho_f}{\rho_s} \right)^2$$

Substitution of the various  $\rho_f/\rho_s$  and  $d_f/d_s$  values into Eq. (36) gives an equation of  $\Delta f/f_0$  in terms of  $E_f/E_s$ . For any range of  $E_f/E_s$  values, the corresponding values of  $\Delta f/f_0$  can be found.



A substrate of Si and a film of Ge have been used. Equation (36) is a general formula and can be used for any combination of materials, but Si and Ge are currently being used in this program. Testing has been conducted on Si wafers 0.02794 cm (0.011 in.) thick with a density of 2.33 g/cc. Young's modulus of the Ge coating is the element of interest in this analysis; its thickness ranges from 1,000 to 3,000 Å and its density from 4.256 to 6.384 g/cc (see Table 5 for details). The coating thickness is in the range of existing coating thicknesses while the 20% variation is used to cover possible density changes. Three thickness ratios of  $3.58 \times 10^{-4}$ ,  $7.16 \times 10^{-4}$ , and  $1.074 \times 10^{-3}$ , and five density ratios of 1.83, 2.05, 2.28, 2.51, and 2.74 are obtained from the data gathered. When these values are substituted into Eq. (34), one obtains fifteen different cases for the  $\Delta f/f_0$  vs.  $E_f/E_s$  relationship. The graphs of the fifteen curves are plotted as three separate graphs with the density ratio varying for each of the three thickness ratios. Each of the three graphs has been plotted with  $\Delta f/f_0$  vs.  $E_f/E_s$ , as depicted in Figs. 22, 23, and 24. The uppermost curve represents a density ratio of 1.83, and with each succeeding curve, the values are 2.05, 2.28, 2.51, and 2.74. Figures 22, 23, and 24 represent thickness ratios of  $2.38 \times 10^{-4}$ ,  $7.16 \times 10^{-4}$ , and  $1.074 \times 10^{-3}$ , respectively.

Table 5. Material Properties

		Film	Substrate	Density Ratio	Thickness Ratio
Density at fractions of bulk, g/cc:	.80	4.256	2.33	1.83	
	.90	4.788		2.05	
	1.00	5.320		2.28	
	1.10	5.852		2.51	
	1.20	6.384		2.74	
Thickness, cm		$1 \times 10^{-5}$	0.02794		$3.48 \times 10^{-4}$
		$2 \times 10^{-5}$			$7.16 \times 10^{-4}$
		$3 \times 10^{-5}$			$1.07 \times 10^{-3}$

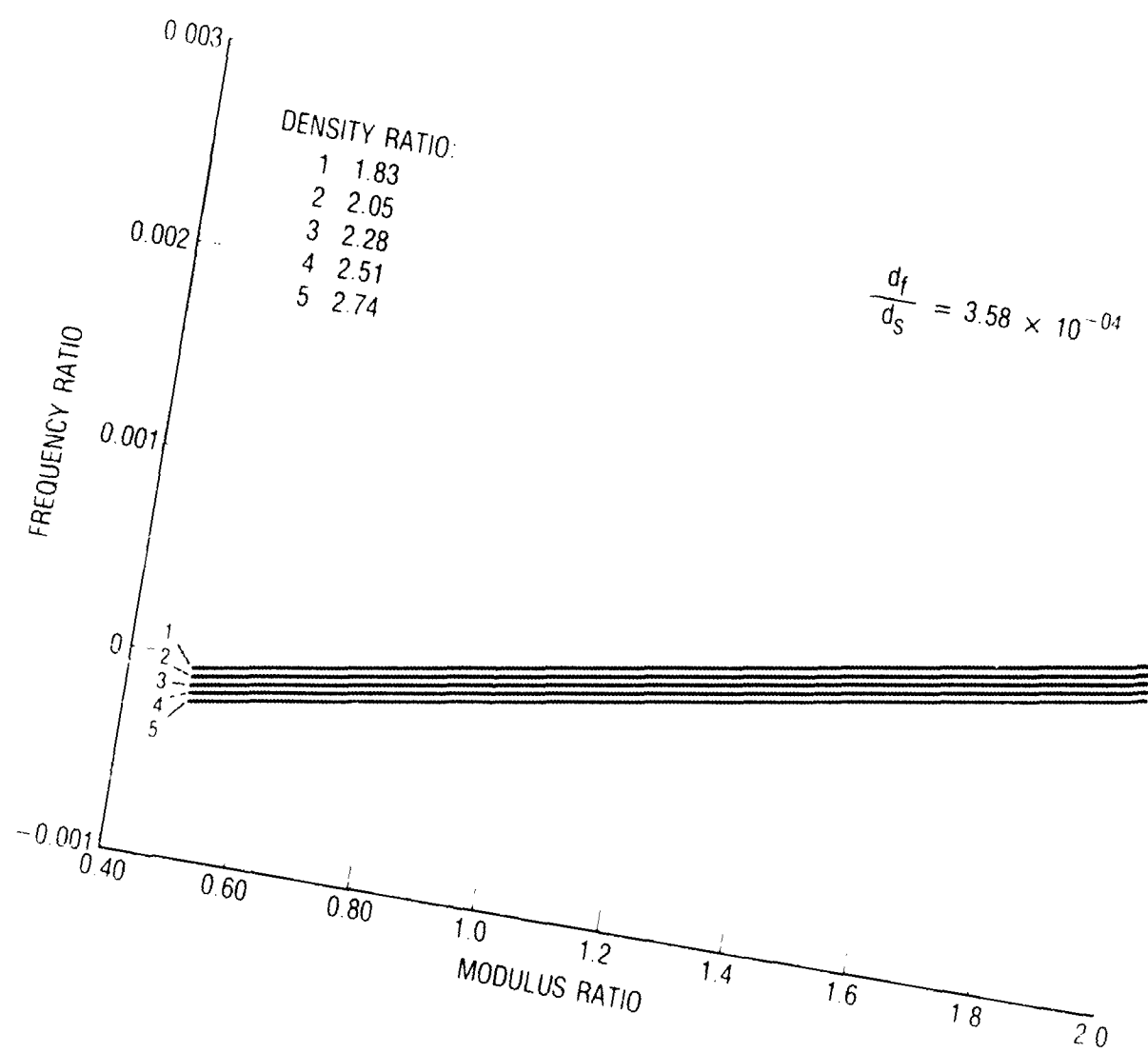


Fig. 22. Frequency Ratio Versus Modulus Ratio

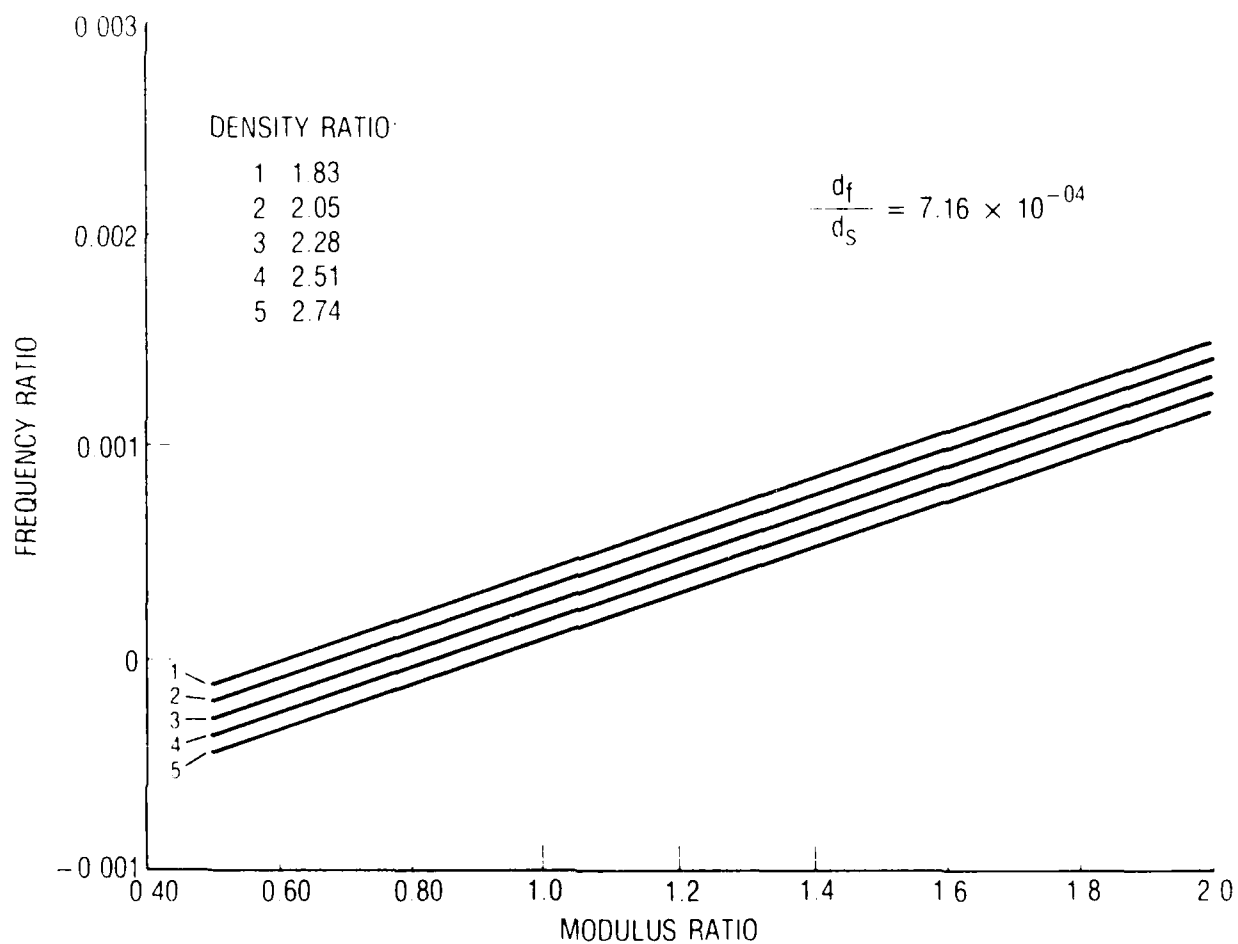


Fig. 23. Frequency Ratio Versus Modulus Ratio

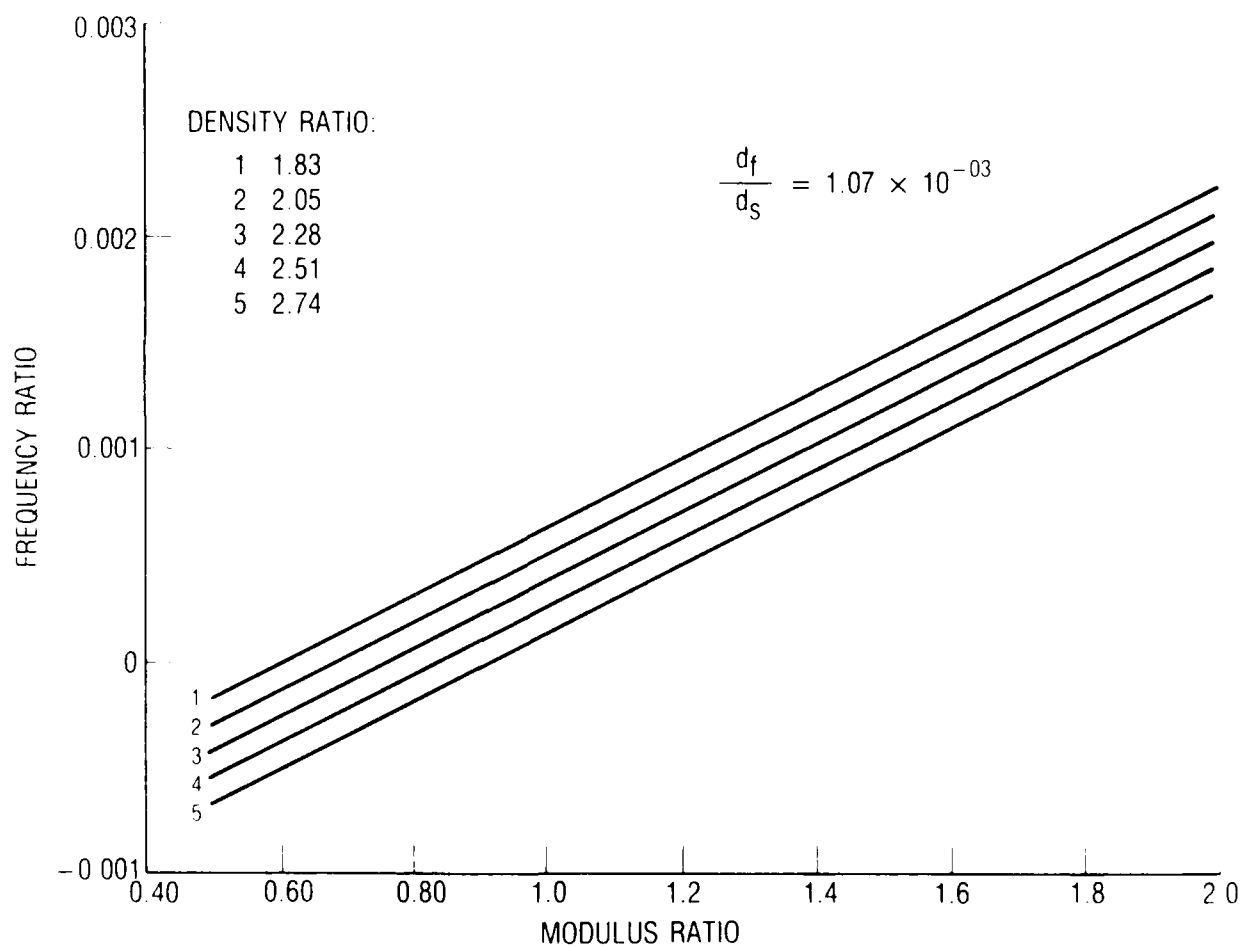


Fig. 24. Frequency Ratio Versus Modulus Ratio,  $d_f/d_s = 1.07 \times 10^{-03}$

Several observations can be interpreted from the equations and the three graphs:

1. For  $d_f/d_s \ll 1$ , the modulus ratio is linearly proportional to the density ratio and the frequency ratio ( $\Delta f/f_0$ ) is linearly proportional to the thickness ratio. For large  $d_f/d_s$  values, the higher order terms of  $d_f/d_s$  will contribute more.
2. If  $d_f/d_s$ ,  $\lambda$  and  $\Delta f/f_0$  remain constant, then a density ratio error of  $\Delta \rho_f/\rho_s$  will result in an error of approximately  $(1/3) \frac{\Delta \rho_f}{\rho_s}$  in the modulus ratio.
3. For a given modulus ratio, increasing the  $d_f/d_s$  ratio results in larger  $\Delta f/f_0$  ratios.
4. When  $E_f/E_s = 0.6$  and  $\rho_f/\rho_s = 1.8$ , or  $\frac{E_f}{E_s} = \frac{1}{3} \frac{\rho_f}{\rho_s}$  in Eq. (34),  $\Delta f/f_0$  is nearly equal to zero. In all of the graphs where  $\Delta f/f_0 = 0$ , the sensitivity of  $E_f/E_s$  is low.

#### B. DETERMINATION OF SHEAR MODULUS

Two independent elastic moduli are needed to characterize the elastic properties of an isotropic material. In this respect, it is essential to characterize the mechanical properties of a coated film by measuring another elastic modulus other than Young's modulus.

The free torsional vibration of a cantilever plate composed of a non-coated substrate is considered. The objective is to determine the shear modulus of the film from the shift of the natural frequency from that for the non-coated to that for the film-coated substrate.

Figure 25 shows geometrical symbols for the cantilever and the choice of coordinates with the x-axis passing through the centroid of each cross section. The analysis was originally carried out for a substrate coated equally on the top and bottom surfaces with the total film thickness  $d_f$ . However, the results obtained hold equally well for the coated substrate with the total film thickness, regardless of the thickness ratio between the films on the top and the bottom surface, if the film-thickness  $d_f$  is much smaller than the substrate-thickness  $d$ .

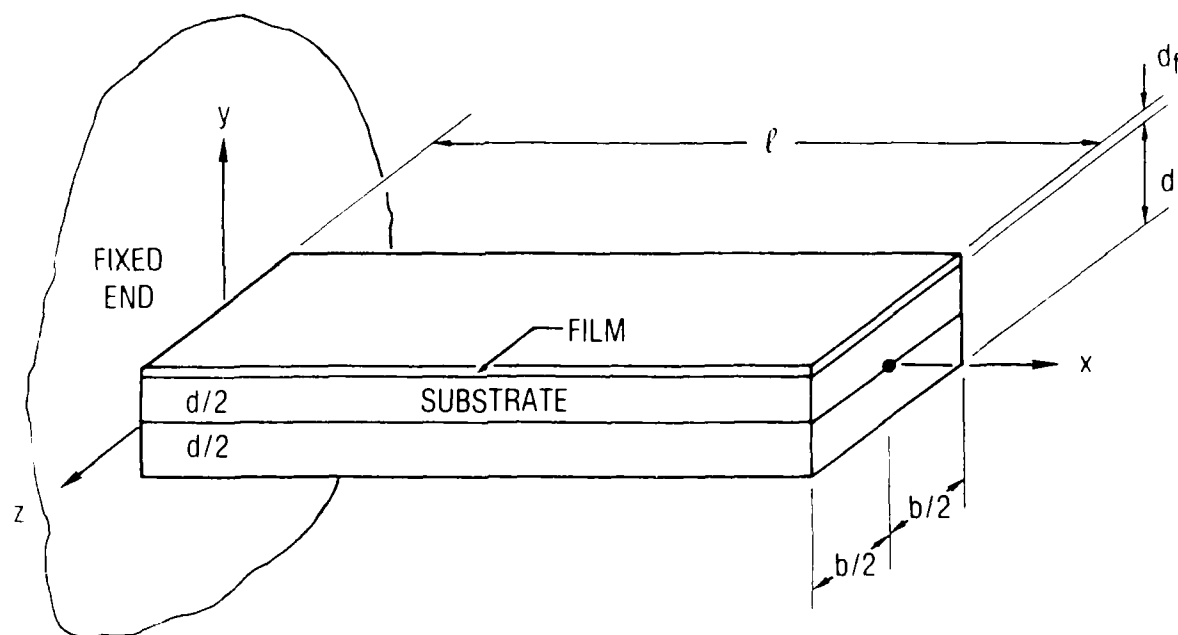


Fig. 25. Geometry and Coordinates

Torsional vibration of a beam is most conveniently described by the angle of twist,  $\theta(x,t)$ , of the cross section. For a cantilever shown on Fig. 25 satisfying

$$d < b \ll l,$$

the torsional vibration is governed by the following eigenvalue problem:

$$(GK + G_f K_f) \frac{\partial^2 \theta}{\partial x^2} = (\rho J + \rho_f J_f) \frac{\partial^2 \theta}{\partial t^2} \quad (37)$$

$$\theta = 0 \quad \text{at } x = 0, \quad \frac{\partial \theta}{\partial x} = 0 \quad \text{at } x = l \quad (38)$$

where symbols without subscript refer to substrate, those with subscript  $f$  to the film,  $G$  the shear modulus,  $\rho$  the density and

$$\begin{aligned} K &= \frac{bd^3}{3}, \quad J = \frac{bd}{12} (b^2 + d^2), \\ K_f &= \frac{bd_f}{3} (d^2 + dd_f + d_f^2) \doteq \frac{bd^2 d_f}{3}, \\ J_f &= \frac{bd_f}{12} (b^2 + 3d^2 + 3dd_f + d_f^2) \doteq \frac{bd_f}{12} (b^2 + 3d^2) \end{aligned} \quad (39)$$

Details of this formulation are presented in the Appendix B.

Now, let  $p$  and  $p_0$  denote the angular frequency for the fundamental mode of the coated and the uncoated substrate, respectively. Further, assume

$$\theta(x,t) = A \sin\left(\frac{\pi}{2} \frac{x}{l}\right) e^{ipt} \quad (40)$$

Substitution of  $\theta$  from (40) into (37) yields, in view of (39)

$$p_0 = \frac{\pi}{l} \left[ \frac{d^2}{b^2 + d^2} \frac{G}{\rho} \right]^{1/2} \quad (d_f = 0) \quad (41)$$

and

$$p = \frac{\pi}{2l} \left[ \frac{GK + G_f K_f}{PJ + \rho_f J_f} \right]^{1/2} \quad (d_f \neq 0) \quad (42)$$

Expand the right hand side of (40) into a power series of  $d_f/d$  by use of (39) and (41) and keep the first two terms to get

$$p = p_o \left[ 1 + \frac{1}{2} \frac{d_f}{d} \left( 3 \frac{G_f}{G} - \frac{b^2 + 3d^2}{b^2 + d^2} \frac{\rho_f}{\rho} \right) \right] \quad (43)$$

$$\Delta p = p - p_o.$$

Then, the shear modulus of the film is determined from (43) in terms of the frequency shift  $\Delta f$  as

$$G_f = \frac{1}{3} \left[ \frac{2\Delta f}{f_o} \frac{d}{d_f} + \frac{b^2 + 3d^2}{b^2 + d^2} \frac{\rho_f}{\rho} \right] G \quad (44)$$

which is the desired result.



## REFERENCES

1. G. G. Stoney, "The Tension of Metallic Films Deposited by Electrolysis," Proc. Roy. Soc., A 32, pp. 172-175 (1909).
2. R. W. Hoffman, "The Mechanical Properties Thin Condensed Films," Physics of Thin Films (ed. G. Hass and R. E. Thun), Vol. 3, pp. 211-273, Academic Press, NY (1966).
3. J. D. Finegan, and R. W. Hoffman, "Stress Anisotropy in Evaporated Iron Films", J. Appl. Phys. 30 597 (1959).
4. A. Brenner, and Sanderoff, "Calculations of Stress in Electrodeposits from the Curvature of the Plated Strip", Journal of Research of the National Bureau of Standards, Research Paper RP 1954 vol. 42 105, 1949.
5. D. J. Chang and R. Muki, "Stress Distribution in a Lap Joint Under Tension-Shear," Int. J. Solids Structures, Vol. 10, pp. 503-517 (1974).
6. H. Blackburn and D. S. Campbell, "The Development of Stress and Surface Temperature During Deposition of Lithium Fluoride Films," Phil. Mag. 8 823 (1963).
7. B. A. Boley and J. H. Weiner, Theory of Thermal Stresses, John Wiley and Sons, New York, 1960.
8. A. Bohg, "Measurements of Stresses in Thin films on Single Crystal Substrates," Phys. Stat. Sol. (a) 4b, 445 (1978).
9. J. P. Den Hartog, Advanced Strength of Materials, McGraw-Hill book Company, Inc. 1982.
10. H. P. Klug and L. E. Alexander, X-ray Diffraction Procedures for Polycrystalline and Amorphous Materials, 2nd edition, John Wiley, New York, 966, 1974.
11. G. A. Rozgonyi and T. J. Ciesielka, "X-ray Determination of Stresses in Thin Films and Substrates by Automatic Bragg Angle Control, Rev. Sci. Instrum. V. 44 (8), p. 1053-7 (1973).
12. A. Bohg and E. Mirbach, Measuring Tensions in Thin Films, IBM Tech. Discl. Bull, #17 (5), p. 1394-5 (1976).
13. W. S. Berry, "Direct Determination of Stress in a Thin Film Deposited on a Single-Crystal Substrate from an X-ray Topographic Image, Advances in X-ray Analysis, V, 26 p. 255-258 (1983).

14. E. W. Hearn, "Stress Measurements in Thin Films Deposited on Single Crystal Substrates through X-ray Topography Techniques," Advances in X-ray Analysis, V 20, p. 273-281 (1977).
15. C. L. Kuo and J. C. Bilello, "Analysis of X-ray Diffraction Conditions for Double-Crystal Topography," J. Appl. Cryst., V. 17, 442-450 (1984).
16. G. R. Jones, I. M. Young, B. Cockayne and G. T. Brown, "X-ray Dispersive Double Crystal Topography," Inst. Phys. Conf. Ser. #60 (5) p. 264-276 (1981).
17. J. W. Beams, Structures and Properties of Thin Films, Wiley, New York (1959).
18. K. Vozumi, H. Honda and A. Kinbana, "Young's Moduli of Vacuum-Deposited Films," Thin Solid Films, v. 37 L49-L51 (1976).
19. F. A. List and R. A. McKee, "Mechanical Properties of Metallic Films on Sapphire," Proceedings of Material Research Society Meeting, Boston, Mass. (Dec. 1985).
20. A. Kikuchi, S. Baba and A. Kinbana, "Internal Stress and Young's Modulus of Vacuum Deposited Germanium Films" (in Japanese) Shinku (Vacuum), V. 24, 259-262 (1981).
21. K. P. Rao and R. K. Gupta, Mechanical Vibration, p. 338 (1984).
22. I. S. Sokolnikoff, Mathematical Theory of Elasticity, p. 132, 2nd edition, (1956).
23. S. Carslaw and J. S. Jaeger, Conduction of Heat in Solids, Oxford University Press, London, 1959.

## APPENDIX A. DERIVATION OF THERMAL DISTRIBUTION AND DEFLECTION

### 1. TEMPERATURE DISTRIBUTION

Temperature distributions in the substrate during and after the coating deposition are well represented by solutions to the one-dimensional heat conduction problem of a slab bounded by planes,  $z = 0$  and  $d$ . At the initial instant, the temperature  $T(z, t)$  is equal to the ambient temperature  $T_0$ . During the coating, we assume that a constant rate of heat flux  $q_0$  per unit area is supplied at the front surface and heat radiates at the rear surface into the surrounding medium of temperature  $T_0$  according to Newton's law with coefficient of surface heat transfer  $H$ . After the end of deposition, it is assumed that the heat radiates from the front and rear planes with a linear initial temperature distribution.

To simplify the formulation of the analysis, we introduce the following dimensionless quantities:

$$\begin{aligned}\xi &= z/d \\ \tau &= \kappa t/d^2 \\ \epsilon &= dH/K\end{aligned}\tag{A1}$$

$$v(\xi, \tau) = [T(z, t) - T_0]/[T_1 - T_0]$$

$$\theta_0 = dq_0/[K(T_1 - T_0)]$$

where  $K$  and  $\kappa$  stand for the conductivity and diffusivity of the substrate, respectively, and  $T_1$  denotes the equilibrium temperature at the front surface when the deposition is continued indefinitely.

In this dimensionless formulation, the heat conduction equation

$$\frac{\partial^2 v}{\partial \xi^2} = \frac{\partial v}{\partial \tau} \quad (0 < \xi < 1, \quad 0 < \tau < \infty) \tag{A2}$$

is determined by, for the deposition problem,

$$\begin{aligned} v_d(\xi, \tau) &= 0 & (0 < \xi < 1), \\ \frac{\partial v_d}{\partial \xi} + \epsilon v_d &= 0 & \text{at } \xi = 0, \\ \frac{\partial v_d}{\partial \xi} + \epsilon v_d &= 0 & \text{at } \xi = 1; \end{aligned} \quad (A3)$$

and similarly, for the post-deposition problem,

$$\begin{aligned} v_p(\xi, 0) &= a + b\xi & (0 < \xi < 1), \\ \frac{\partial v_p}{\partial \xi} - \epsilon v_p &= 0 & \text{at } \xi = 0, \\ \frac{\partial v_p}{\partial \xi} + \epsilon v_p &= 0 & \text{at } \xi = 1. \end{aligned} \quad (A4)$$

The terms  $v_d$  and  $v_p$  denote the solutions to the deposition and the post-deposition problems, respectively. Expressions representing them can be obtained by such standard procedure<sup>(23)</sup> as the Laplace transform:

$$v_d(\xi, \tau) = B_0 \left(1 + \frac{1}{\epsilon} - \xi\right) - 4\epsilon B_0 \sum_{n=1}^{\infty} \frac{e^{-\lambda_n^2 \tau} \cos(\lambda_n \xi)}{\lambda_n [\lambda_n^2 + \epsilon(1 + \epsilon)] \sin(2\lambda_n)}, \quad (A5)$$

where

$$\lambda_n \tan \lambda_n = \epsilon \quad (A6)$$

and

$$\begin{aligned} v_p(\xi, \tau) &= 4\epsilon \left(a + \frac{b}{2}\right) \sum_{n=1}^{\infty} \frac{e^{-4\kappa_n^2 \tau} \cos[2\kappa_n(\xi - 1/2)]}{[4\kappa_n^2 + \epsilon(2 + \epsilon)] \cos \kappa_n} \\ &\quad + 4\left(1 + \frac{\epsilon}{2}\right)b \sum_{n=1}^{\infty} \frac{e^{-4\gamma_n^2 \tau} \sin[2\gamma_n(\xi - 1/2)]}{[4\gamma_n^2 + \epsilon(2 + \epsilon)] \sin \gamma_n}, \end{aligned} \quad (A7)$$

where

$$\kappa_n \tan \kappa_n = \frac{\epsilon}{2} \quad \text{and} \quad \gamma_n \cot \gamma_n = -\frac{\epsilon}{2}. \quad (\text{A8})$$

Equations (A5) and (A7) involve infinite series. Their convergence becomes slow when they are used for very small  $\tau$  values. Expressions suitable for small  $\tau$  values are established by asymptotic inversion of the transformed solution. We list here only the expression for  $v_d$

$$v_d(\xi, \tau) = 2B_0 \tau^{1/2} \text{ierfc} \left( \frac{\xi}{2\tau^{1/2}} \right) - 2B_0 L(2 - \epsilon, \tau) - 2B_0 L(2 + \xi, \tau) + \dots \quad (\text{A9})$$

where

$$\begin{aligned} \text{ierfc}(x) &= \frac{1}{\pi^{1/2}} e^{-x^2} - x \text{erfc } x, \\ L(\xi, \tau) &= \tau^{1/2} \text{ierfc} \left( \frac{\xi}{2\tau^{1/2}} \right) + \frac{1}{\epsilon} \exp(\epsilon\xi + \epsilon^2\tau) \text{erfc} \left( \frac{\xi}{2\tau^{1/2}} + \epsilon\tau^{1/2} \right) \\ &\quad - \frac{1}{\epsilon} \text{erfc} \left( \frac{\xi}{2\tau^{1/2}} \right). \end{aligned} \quad (\text{A10})$$

It is observed from Eq. (A5) that the steady state temperature demands a constrained relation

$$B_0 = \frac{\epsilon}{1 + \epsilon}, \quad (\text{A11})$$

which is the consequence of Eq. (A1) and  $\lim_{\tau \rightarrow \infty} v_d(0, \tau) = 1$ .

In ordinary coating-depositions, the parameter  $\epsilon$  is extremely small. For such cases, the roots  $\lambda_n, \kappa_n$ , and  $\gamma_n$  of transcendental Eqs. (A6) and (A8) are closely approximated by

$$\lambda_1 = \epsilon^{1/2} \left(1 - \frac{\epsilon}{6}\right), \quad \lambda_n = (n-1)\pi + \epsilon/[2(n-1)\pi] \quad (A12)$$

(n = 2, 3, ...),

$$\kappa_1 = \frac{\epsilon^{1/2}}{2^{1/2}} \left(1 - \frac{\epsilon}{12}\right), \quad \kappa_n = (n-1)\pi + \epsilon/[2(n-1)\pi] \quad (A13)$$

(n = 2, 3, ...),

$$\lambda_n = (2n-1) \frac{\pi}{2} + \epsilon/[2(2n-1)\pi] \quad (n = 1, 2, \dots). \quad (A14)$$

When  $\epsilon \ll 1$ , simple asymptotic expressions for  $v_d$  and  $v_p$  are obtained from Eqs. (A5) and (A7), respectively, after the use of Eqs. (A11) through (A14):

$$v_d(\xi, \tau) = 1 - e^{-\epsilon\tau} - \epsilon \left[ \xi - \left( \frac{1}{3} + \frac{\xi^2}{2} \right) e^{-\epsilon\tau} \right], \quad (A15)$$

$$v_p(\xi, \tau) = \left( a + \frac{b}{2} \right) \left( 1 + \frac{\epsilon}{12} \right) \left[ 1 - \epsilon \left( \xi - \frac{1}{2} \right)^2 \right] e^{-2\epsilon\tau}$$

$$+ \frac{4b}{\pi^2} \sin[(\xi - 1/2)\pi] e^{-\pi^2\tau}. \quad (A16)$$

These expressions supply satisfactory values except for very small  $\tau$ .

## II. THERMAL DEFLECTION

Once the temperature in a substrate is determined, the thermal deflection can be predicted. To calculate the thermal deflection, it is assumed that a circular wafer of radius  $a$ , thickness  $d$  and coefficient of thermal expansion  $\alpha$  experiences temperature variation  $T(z)$  across the thickness over a concentric circular region of radius  $b$ . It is further assumed that the boundary is simply supported. From the known solution<sup>7</sup>, the deflection at the center is obtained as

$$w(0) = \frac{6\alpha b^2}{d^3} [1 - (1 + \nu) \log(b/a)] \int_0^d T(z)(z - d/2) dz. \quad (A17)$$

The tip-deflection of a cantilever plate of length  $l$  with the temperature distribution  $T(z)$  across the thickness is known to be

$$\delta = - \frac{6\alpha l^2}{d^3} \int_0^d T(z)(z - d/2) dz. \quad (A18)$$

In view of Eq. (A17), the integral in Eqs. (A18) and (18) can be written in terms of the dimensionless temperature [Eq. (A1)] as

$$\int_0^d T(z)(z - d/2) dz = (T_1 - T_0) d^2 \int_0^1 V(\xi, \tau)(\xi - 1/2) d\xi. \quad (A19)$$

# APPENDIX B. DERIVATION OF EQUATIONS (37) AND (38)

We follow the formulation procedure adopted by Rao and Gupta<sup>21</sup> for the torsional vibration of a cantilever plate and take the correction due to the coating film into account.

Assume the displacement field as

$$U_x = \phi\theta_{,x}, U_y = -z\theta, U_z = y\theta \quad (B1)$$

where  $\phi(y,z)$  denotes warping of the cross section per rate of twist and the subscript  $x$  preceded by a comma represents differentiation with respect to  $x$ . This rule will also apply to all space and time variables. Substitution of displacements from Eq. (B1) into the strain-displacement relation leads to

$$\begin{aligned} \epsilon_{xx} &= \phi\theta_{,xx}, & \epsilon_{yy} &= \epsilon_{zz} = 0 \\ \epsilon_{xy} &= \frac{1}{2}(\phi_{,y} - z)\theta_{,x}, & \epsilon_{yz} &= 0 \\ \epsilon_{xz} &= \frac{1}{2}(\phi_{,z} + y)\theta_{,x} \end{aligned} \quad (B2)$$

Stresses in the substrate associated with strain (B2) are

$$\begin{aligned} \sigma_{xx} &= E\phi\theta_{,xx}, & \sigma_{yy} &= \sigma_{zz} = \sigma_{yz} = 0, \\ \sigma_{xy} &= G(\phi_{,y} - z)\theta_{,x}, & \sigma_{xz} &= G(\phi_{,z} + y)\theta_{,x}. \end{aligned} \quad (B3)$$

Stresses in the film will be obtained from (B3) by replacing  $E$  and  $G$  by  $E_f$  and  $G_f$ ; these equations will be referred to as (B<sub>f</sub>3).

The boundary conditions for the cantilever plate are

$$\begin{aligned} U_y = U_z = 0, & & \sigma_{xx} = 0 & & \text{at } x = 0 \\ \sigma_{xy} = \sigma_{xz} = 0, & & \sigma_{xx,x} = 0 & & \text{at } x = l \end{aligned} \quad (B4)$$



$$\begin{aligned}
\theta &= 0, & \theta_{,xx} &= 0 & \text{at } x &= 0 \\
\theta_{,x} &= 0, & \theta_{,xxx} &= 0 & \text{at } x &= l
\end{aligned}
\tag{B5}$$

We then calculate the strain energy and the kinetic energy of the system and appeal to Hamilton's principle to arrive at the governing differential equation:

$$\begin{aligned}
(EI + E_f I_f) \theta_{,xxxx} - (GK + G_f K_f) \theta_{,xx} \\
- (\rho I + \rho_f I_f) \theta_{,xxtt} + (\rho J + \rho_f J_f) \theta_{,tt} = 0
\end{aligned}
\tag{B6}$$

where

$$\begin{aligned}
I &= \iint_A \phi^2 dA, & K &= \iint_A [\phi_{,y} - z]^2 + (\phi_{,z} + y)^2 dA, \\
J &= \iint_A (y^2 + z^2) dA
\end{aligned}
\tag{B7}$$

while the expressions for  $I_f$ ,  $K_f$ ,  $J_f$  to be called as  $(B_f7)$  are obtained from (B7) by replacing  $A$  by  $A_f$  in which

$$\begin{aligned}
A &= \{y, z \mid -\frac{d}{2} \leq y \leq \frac{d}{2}, \quad -\frac{b}{2} \leq z \leq \frac{b}{2}\} \\
A_f &= \{y, z \mid \frac{d}{2} < |y| \leq \frac{1}{2}(d + d_f), \quad -\frac{b}{2} \leq z \leq \frac{b}{2}\}
\end{aligned}
\tag{B8}$$

If our interest is to find the fundamental frequency, we may assume the mode shape as given by Eq. (42). Substitution of  $\theta$  from Eq. (40) into Eq. (B6) shows that the first and the third term in Eq. (B6) can be neglected when  $b \ll l$ . Therefore, the original problem with the differential Eq. (B6) and the boundary conditions Eq. (B5) can be replaced by a simpler problem consisting of the second order equation (Eq. 37) and the boundary conditions Eq. (38).

For thin rectangular cross section ( $d < b$ ), the warping function is approximately given by (Ref. 22).

$$\phi(y,z) = yz \quad (B9)$$

Then, expressions for  $K$ ,  $J$ ,  $K_f$  and  $J_f$  are evaluated from (B7), (B7) and (B8) as given in (37).

The analysis in the Appendix has been carried out for the case where the film is deposited on the top and the bottom surface of the substrate by an equal thickness  $d_f/2$ . On the other hand, the final results, (41) and (42), refer to the case where the film is deposited only on the top surface. It is to be pointed out here that these results, (41) and (42), hold true regardless of the ratio of films on the top and the bottom surfaces since the effect of such ratio appears only for the higher order terms of  $d_f/d$ , not the first two terms of the Taylor series expansion in (41).

## 1. AWFAL'S ORIGIN

AWFAL's origin stems from the need for an efficient means for the development, testing, and validation of military space systems. In the early 1970's, partly the participation of national laboratories in the research and the technical investigations that have led to the application of space technology to various systems, and partly the success of the investigations as the technical staffs with training expertise and its ability to deal with new developments. This expertise is enhanced by the fact that it is directly dealing with the same problems associated with the development of space systems. Contrasting their capabilities to the capabilities of these national laboratories:

Avionics Laboratory: Launch vehicle and reaction fluid reactions; heat transfer and fluid dynamics; chemical and electric propulsion; propellant storage; orbital dynamics; environmental chemistry; trace detection; structural mechanics; contamination; thermal and structural analysis; high temperature thermodynamics; gas kinetics; radiation; low and high power laser development including chemical kinetics; spectroscopy; optical resonators; beam control; atmospheric propagation; laser effects and countermeasures.

Chemistry and Physics Laboratory: Atmospheric chemical reactions, atmospheric optics, light scattering, state-specific chemical reactions and radiative structures of missile plumes; sensor out-of-field-of-view reaction; applied laser spectroscopy; laser chemistry; laser optoelectronics; solar cell physics; battery electrochemistry; space vacuum and radiation effects on materials; ionization and surface phenomena; thermionic emission; photoconductive materials and detectors; atomic frequency standards; and environmental chemistry.

Computer Science Laboratory: Program verification, program translation, computer sensitive system design, distributed architectures for spaceborne computers, fault tolerant computer systems, artificial intelligence, error control, communications, communication protocols, and computer security.

Electronic Research Laboratory: Microelectronics, solid-state device physics, diode and semiconductor, radiation hardening, electronics, quantum electronics, solid-state lasers, optical propagation and communications, microwave semiconductor devices, microwave millimeter wave measurements, microwave radiometry, microwave millimeter wave thermionic devices, atomic time and frequency standards, antennas, rf systems, electromagnetic propagation phenomena, space communication systems.

Materials Sciences Laboratory: Development of new materials: metals, alloys, ceramics, polymers, and their composites, and new forms of carbon; non-destructive evaluation; component failure analysis and reliability; fracture mechanics; stress corrosion analysis and evaluation of materials at cryogenic and elevated temperatures as well as in space and enemy-induced environments.

Space Sciences Laboratory: Magnetospheric, auroral and cosmic ray physics; X-ray auroral interactions; magnetospheric plasma waves; atmospheric and ionospheric physics; density and composition of the upper atmosphere; remote sensing using atmospheric radiation; solar physics; infrared astronomy; infrared signature analysis; effects of solar activity; magnetic storms and magnetic excursions in the earth's atmosphere, ionosphere and magnetosphere; effects of electromagnetic and particulate radiations on space systems; space instrumentation.

END

DATE

FILM

DTIC

7-85